Mechanical Stress Acts via Katanin to Amplify Differences in Growth Rate between Adjacent Cells in *Arabidopsis*

Magalie Uyttewaal,[1,3,7] Agata Burian,[4,7] Karen Alim,[5,7] Benoît Landrein,[1,2] Dorota Borowska-Wykręt,[4] Annick Dedieu,[1] Alexis Peaucelle,[3,6] Michał Ludynia,[4] Jan Traas,[1] Arezki Boudaoud,[1,2,*] Dorota Kwiatkowska,[4,*] and Olivier Hamant[1,2,*]

[1]Laboratoire de Reproduction et Développement des Plantes, INRA, CNRS, ENS, UCB Lyon 1
[2]Laboratoire Joliot Curie, CNRS, ENS Lyon, Université de Lyon
46 Allée d'Italie, 69364 Lyon Cedex 07, France
[3]Institut Jean-Pierre Bourgin, UMR1318 INRA-AgroParisTech, Centre de Versailles, 78026 Versailles Cedex, France
[4]Department of Biophysics and Morphogenesis of Plants, University of Silesia, Jagiellońska 28, 40-032 Katowice, Poland
[5]School of Engineering and Applied Sciences, Harvard University, Cambridge, MA 02138, USA
[6]Université Paris Diderot, UFR de Physique de Paris 7, 75205 Paris, France
[7]These authors contributed equally to this work
*Correspondence: arezki.boudaoud@ens-lyon.fr (A.B.), dorota.kwiatkowska@us.edu.pl (D.K.), olivier.hamant@ens-lyon.fr (O.H.)
DOI 10.1016/j.cell.2012.02.048

SUMMARY

The presence of diffuse morphogen gradients in tissues supports a view in which growth is locally homogenous. Here we challenge this view: we used a high-resolution quantitative approach to reveal significant growth variability among neighboring cells in the shoot apical meristem, the plant stem cell niche. This variability was strongly decreased in a mutant impaired in the microtubule-severing protein katanin. Major shape defects in the mutant could be related to a local decrease in growth heterogeneity. We show that katanin is required for the cell's competence to respond to the mechanical forces generated by growth. This provides the basis for a model in which microtubule dynamics allow the cell to respond efficiently to mechanical forces. This in turn can amplify local growth-rate gradients, yielding more heterogeneous growth and supporting morphogenesis.

INTRODUCTION

A major issue in developmental biology is how reproducible shapes can emerge from the collective behavior of individual cells. This reproducibility implies the existence of some level of growth coordination between individual cells. Mechanistically, it has been proposed that growth patterns rely on morphogen gradients, which orchestrate the growth of individual cells in tissues (Jaeger et al., 2008; Wolpert, 1969). Morphogen gradients have been observed in several systems, and their shape and origin are rather well described (Wartlick et al., 2009).

In addition, growth is a physical process, and physical parameters have also been implicated in the coordination of growth. In particular, in tissues where cells adhere to each other, like imag-inal discs in *Drosophila* or plant tissues (Jarvis et al., 2003), differential growth between neighboring cells is a source of residual mechanical stresses. There is even evidence that stresses themselves act as instructional signals, generating responses in the form of gene expression or cytoskeletal reorganization, in parallel to biochemical gradients (Farge, 2003; Hamant et al., 2008; Lecuit and Lenne, 2007; Shraiman, 2005). Mechanosensitive deformable proteins have been isolated, and patterns of forces have been involved in key physiological and developmental processes (e.g., Fink et al., 2011; Grashoff et al., 2010; Landsberg et al., 2009; Théry et al., 2007; Vogel and Sheetz, 2006). For instance, an active role of mechanical forces in orchestrating cell proliferation patterns in imaginal discs from *Drosophila* has been theorized, but the exact mechanism behind it remains unknown (Aegerter-Wilmsen et al., 2007; Hufnagel et al., 2007; Shraiman, 2005).

Here we examine growth control in plants, where growth patterns depend on cell-wall synthesis and anisotropy (the existence of directions with distinctive properties). More specifically, growth anisotropy is generally larger in the direction perpendicular to the orientation of stiff cellulose microfibrils in the cell wall, which in turn is controlled by the orientation of the cortical microtubule (CMT) arrays that guide the trajectories of cellulose synthase (Paredez et al., 2006). The formation of parallel CMTs is itself thought to be largely self-organized, as microtubule dynamics facilitate encounters, bundling, and microtubule growth in parallel orientations. In this respect, the microtubule-severing protein katanin was proposed to increase the ability of microtubules to self-organize in parallel arrays, by enhancing CMT dynamics and promoting their encounters (Allard et al., 2010; Dixit and Cyr, 2004; Shaw et al., 2003; Wasteneys and Ambrose, 2009).

Interestingly, there is now strong evidence showing that the predominant orientations of the CMTs depend on force fields (Cleary and Hardham, 1993; Green and King, 1966; Hamant et al., 2008; Williamson, 1990; Wymer et al., 1996).
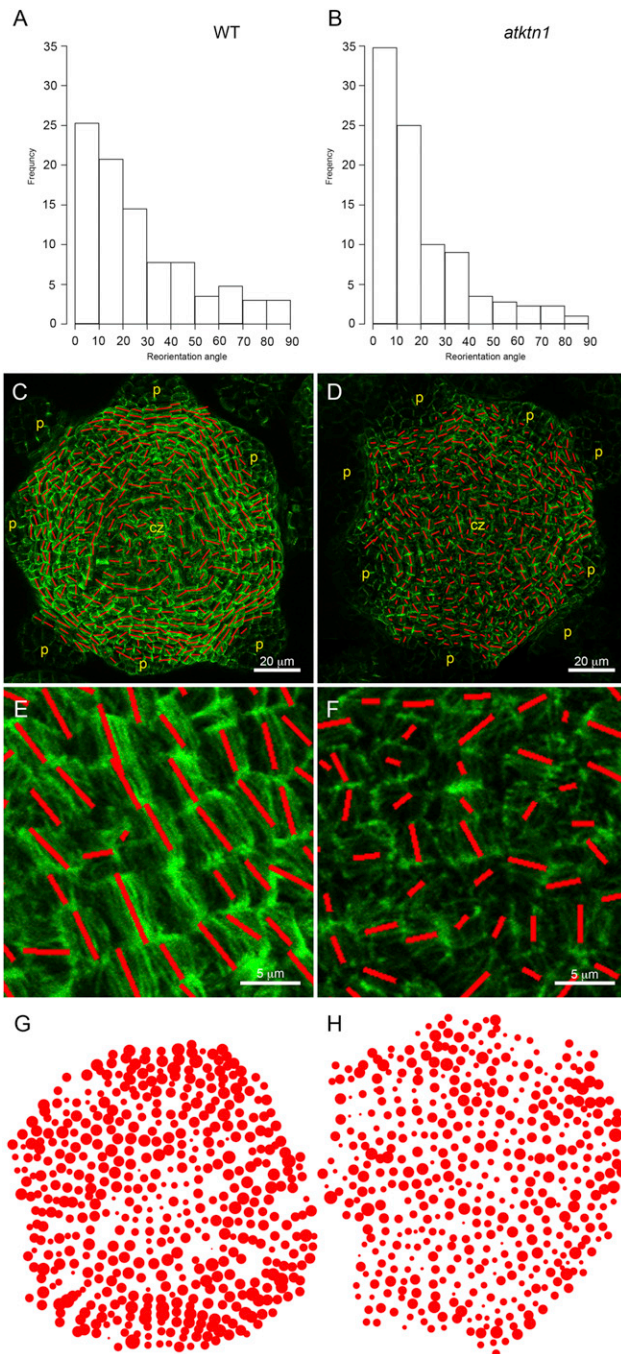
Figure 1. Impaired Supracellular Microtubule Patterning in *atktn1* SAMs

(A and B) The reorientation angle corresponds to the difference between the average CMT angle in a given cell at t0 and 20 min later. The distributions of reorientation angle were weighted by CMT anisotropy (weighted histograms using the R software) in the WT (A, n = 200) and *atktn1* (B, n = 201). Quantifications were restricted to cells from the CZ.

(C and D) *p35S::GFP-MBD* expression at the surface of a representative WT (C) and *atktn1* (D) meristem (CZ: central zone; p: flower primordium). CMT orientation and anisotropy were determined with the MT macro: the orientation and length of the red line in each cell indicate the average CMT orientation and anisotropy of the array, respectively.

More specifically, in the *Arabidopsis* shoot apical meristem (SAM), a tissue that contains the plant stem cell niche and provides the precursor cells for all the postembryonic aerial organs, CMTs modify their orientation toward the direction of maximal stress (Hamant et al., 2008). However, the role of the regulation of the CMT dynamics in this response to stress has not been addressed.

Here we show that the microtubule-severing protein katanin is required to orchestrate growth between neighboring cells by providing cells with the ability to respond efficiently to mechanical stress.

RESULTS

An Impaired Supracellular Microtubule Pattern in *atktn1*

To investigate the role of CMT dynamics in the SAM, we selected the *katanin* (*atktn1*) mutant, which exhibits decreased microtubule dynamics (Bichet et al., 2001; Burk et al., 2001; Burk and Ye, 2002; Nakamura et al., 2010; Stoppin-Mellet et al., 2006; Wasteneys and Ambrose, 2009). The GFP-microtubule-binding domain marker (*GFP-MBD*) was introgressed in the *atktn1* mutant, and the GFP signal was analyzed. To quantitatively monitor the average orientation and anisotropy of CMT arrays in each cell, we generated a macro tool in ImageJ using the nematic tensor concept from the physics of liquid crystals (MT macro, see Extended Experimental Procedures). This allowed us to determine that CMTs reorient more slowly in the mutant than in the wild-type (WT) (Figures 1A and 1B), confirming lower CMT dynamics in *atktn1* cells.

The WT SAM exhibited a binary CMT pattern, with a rather poor CMT organization in the central zone (CZ) and circumferential orientation of CMTs in the peripheral zone (PZ) (Hamant et al., 2008; Sakaguchi et al., 1988) (Figures 1C and 1E). This pattern was strongly affected in the *atktn1* mutant. In particular, although some supracellular CMT alignment could be observed in the boundary domains, it was often difficult to observe any coherent pattern in the PZ of the SAM (Figures 1D and 1F). More generally, the anisotropy of the CMT arrays was 28% lower in the *atktn1* mutant than in the control (mean ± standard error of the mean [SEM] is 0.150 ± 0.001 for the *GFP-MBD* line, standard deviation [SD]: 0.066, n = 2,152 cells; and 0.108 ± 0.001 for the mutant, SD: 0.055, n = 2,128 cells; 5 meristems per genotype; significant difference shown by t test at p < 0.001). Consistent with these CMT defects, cell division planes were also affected in the *atktn1* mutant (Figure S1 available online).

To get a quantitative view of these defects in space, we generated maps in which the CMT array anisotropy is represented as a disc, the radius of which increases with CMT anisotropy (Figures 1G and 1H). In the WT background, this representation clearly distinguished the CZ with nearly isotropic CMT arrays from the PZ with highly anisotropic arrays (Figure 1G). In the

(E and F) Close-ups from (C) and (D) in the PZ of WT (C) and *atktn1* (D) meristems.

(G and H) Spatial distribution of the CMT anisotropy in GFP-MBD (G) and *atktn1* GFP-MBD (H) meristems, the same as those shown at (C) and (D). The diameter of the disc increases with CMT anisotropy.

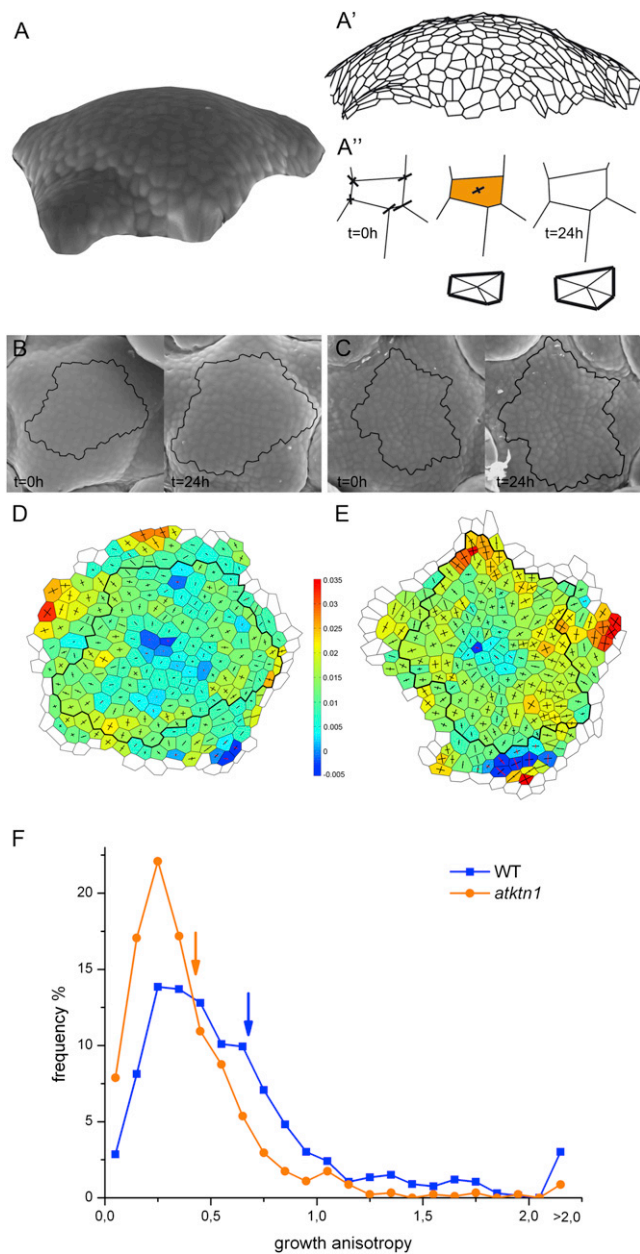**Figure 2. Growth Analysis in *atktn1***

(A–A") Stereoscopic reconstruction (A–A') and computation of growth variables (A") based on the scanning electron microscopy micrographs. Cell-wall pattern at the beginning and at the end of a time interval is used to compute directions of maximal and minimal growth rates, represented by crosses, for all the vertices of a cell and plotted on the cell-wall pattern as it appeared at the first time point (A"). These crosses are averaged to compute directions of maximal and minimal growth for the cell (A"). Growth rate in area of the cell is computed either as a sum of its minimal and maximal growth rates (color-coded in A" upper row—vertex approach) or by comparing the cell surface area, i.e., the sum of triangles, at the two time points (A" lower row—polygon approach) (see Extended Experimental Procedures).

(B–E) Scanning electron micrographs and growth rate maps of WT (B and D) and *atktn1* (C and E) meristems. Replicas from the same meristem were taken at two different time points (0 hr and 24 hr later). Black outlines indicate the SAM region excluding boundaries and flower primordia. The color map

atktn1 mutant, the difference between CZ and PZ was significantly reduced (Figure 1H).

Microtubule Defects in *atktn1* Reduce Growth Anisotropy

To check the impact of the CMT defects in *atktn1* on growth, we next quantified rate of growth in area as well as growth anisotropy (i.e., the unique directions of maximal and minimal values of growth, also called principal directions of growth) of the epidermal cells.

To obtain the highest possible resolution, we used a live scanning electron microscopy protocol, also called the sequential replica method (Dumais and Kwiatkowska, 2002; Williams and Green, 1988; Williams et al., 1987). Briefly, dental polymer molds of WT and *atktn1* meristems were taken at different time points, and replicas of the meristems in epoxy resin were obtained and imaged with scanning electron microscopy, at two different angles, in order to position each cell vertex in three dimensions (3D) and compute growth rates and anisotropy (Dumais and Kwiatkowska, 2002; Routier-Kierzkowska and Kwiatkowska, 2008) (Figures 2A–2E).

As expected from the CMT pattern, we observed a decrease in growth anisotropy in all *atktn1* SAMs analyzed, when compared to the WT. The growth anisotropy was 37% lower in the *atktn1* mutant than in the control (mean ± SEM is 0.67 ± 0.03 for the WT, n = 664 cells, and 0.42 ± 0.02 for the mutant, n = 912 cells; 6 meristems per genotype; significant difference shown by t test at p < 0.001; Figure 2F). In contrast, no clear difference in terms of rate of growth in area could be observed between the WT and *atktn1* on the SAM surface at first sight (Figures 2D and 2E). Discriminating between the WT and the mutant growth patterns was also difficult because of variability between individual meristems (Figure S2).

The SAM Exhibits a Crater-like Shape in *atktn1*

Several morphogenetic features were altered in the *atktn1* mutant. More specifically, the *atktn1* meristems were flatter, and their surface was slightly bumpy, with a notable crater-like depression at the center of the meristem (Figures 3A and 3B). We quantified this morphology with the replica method (Figures 3A–3C and S3; Extended Experimental Procedures). More specifically, the principal curvature directions at the cell centroid, i.e., the directions in which the normal curves lying on the surface attain maximal or minimal value, were computed as described previously (Dumais and Kwiatkowska, 2002; see Extended Experimental Procedures). The curvature was negative in both curvature directions in the center of the *atktn1* SAM

(D and E) shows the growth rate in area in h^{-1} (vertex approach, see Extended Experimental Procedures for details). The orientation and length of cross arms represent the directions and values of principal growth rates (maximal and minimal growth rates). The arms appear in red if negative growth rate (contraction) occurs.

(F) Distribution of growth anisotropy for the WT and *atktn1* SAM cells. Data were extracted from the growth rate maps, for n = 664 cells (six meristems) of WT and n = 912 cells (six meristems) of *atktn1*. Arrows indicate the mean growth anisotropy for WT (blue) and *atktn1* (orange). The distributions and means for WT and *atktn1* are significantly different (Kolmogorov-Smirnov test, p < 0.001; and t test, p < 0.001).
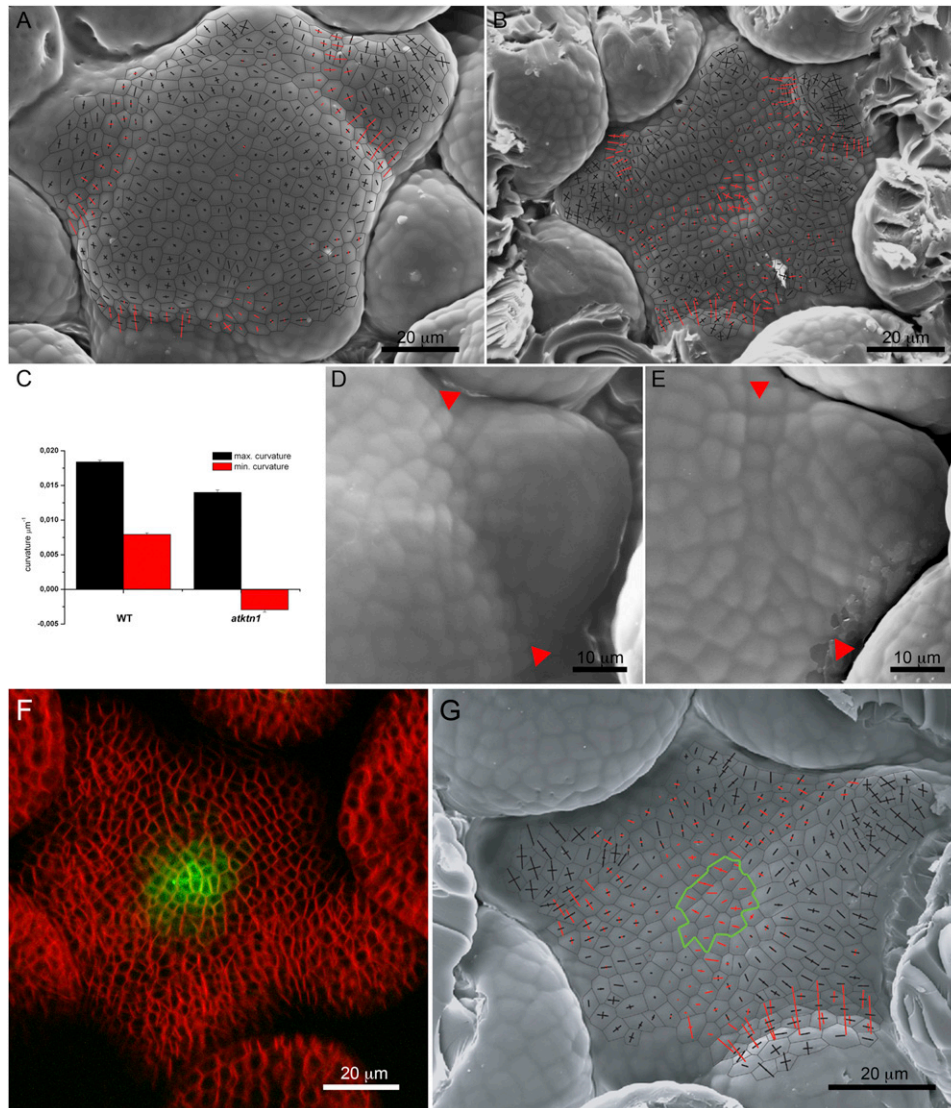
Figure 3. Geometry of *atktn1* Meristems in Comparison with WT

(A and B) Scanning electron micrographs with overlaid principal curvature directions for WT (A) and *atktn1* (B) meristems. The orientation and length of cross-arms represent the direction and value of principal curvatures. The arm appears in red if in this direction the surface is concave (negative curvature) and in black when the surface is convex (positive curvature).

(C) Mean values of maximal and minimal curvatures computed for WT and *atktn1* SAM cells. Error bars are SEM. Plants were grown in the Lyon laboratory conditions (see Extended Experimental Procedures). The means computed for n = 712 cells (four meristems) of WT and n = 934 cells (four meristems) of *atktn1* are significantly different (t test, p < 0.001).

(D and E) Close-ups showing the primordia boundary domains (between red arrowheads) in WT (D) and *atktn1* (E) at the similar plastochron age.

(F) *pCLV3::AlcR AlcA::GFP* expression after ethanol induction in a *atktn1* FM4-64-stained (red) meristem.

(G) Scanning electron micrograph with overlaid curvature map of the *pCLV3::AlcR AlcA::GFP atktn1* meristem shown in (F). The GFP expression domain is outlined in green.

(Figures 3A–3C). Tissue folding at the boundaries was also less sharp in the *atktn1* mutant than in the WT (Figures 3D and 3E). Notably, whereas concave curvature (red arms on Figures 3A and 3B) usually encompassed a two-cell file domain in WT boundaries, it covered the width of three to four cell files in the *atktn1* mutant.

To check whether the position of the depression in the *atktn1* SAM corresponds to that of the CZ, we introgressed the CZ marker *pCLV3::GFP* into the *atktn1* mutant. Using a combined confocal-scanning electron microscopy protocol, we observed that the position of the depression in *atktn1* matched that of the *pCLV3::GFP* expression domain (Figures 3F and 3G). Given that the CZ is growing slower than the PZ in both the WT and the *atktn1* mutant (Figures 2D and 2E), the crater shape observed in the *atktn1* mutant could be due to defects in growth anisotropy in the PZ.

Indirect Evidence for a Decreased Response to Mechanical Stress in the *atktn1* Mutant

Previous data support a model in which CMTs orient according to the maximal mechanical stress direction, and this direction is largely determined by tissue shape (Hamant et al., 2008; Heisler et al., 2010). Although the mechanoperception pathway behind it remains to be identified (Mirabet et al., 2011; Monshausen and Gilroy, 2009), it was shown that CMT orientations better match stress patterns than strain patterns (Hamant et al., 2008): strain measures the intensity and direction of material deformation (i.e., cell growth), whereas stress measures the intensity and direction of mechanical forces in cells, normalized by the geometrical features of the material (here the thickness of the cell wall). CMTs usually are perpendicular to the maximal strain direction, and parallel to the predicted maximal stress direction in cells. In the boundary domain of the SAM or after applying local forces onto the SAM, CMTs become parallel to the maximal direction of both stress and strain. In the following, we used the *atktn1* mutant to investigate whether this mechanical feedback is altered when microtubule dynamics is affected.

The presence of supracellular CMT alignments is regarded as a landmark for the response of microtubules to mechanical stress (Hamant et al., 2008). In this framework, the presence of disorganized CMTs in *atktn1* could potentially be explained by lower stress levels in *atktn1*. However, bending tests, breaking force, and tensile modulus measurements as well as wall thickness analyses all point at weaker walls in differentiated tissues of *atktn1* alleles, thus suggesting that stress levels should instead be increased in the mutant (Bichet et al., 2001; Burk et al., 2001; Burk and Ye, 2002; Ryden et al., 2003). Using a microvice, we first compressed WT and *atktn1* meristems to obtain a rough estimate of the mechanical properties of this tissue (see Extended Experimental Procedures). The response was similar in both genotypes, suggesting that stress levels were comparable. To check this at a more local level, with a recently published protocol, we used atomic force microscopy to measure the apparent elastic moduli of meristematic cells in WT and *atktn1* (Peaucelle et al., 2011). This analysis revealed that *atktn1* cell walls in the SAM were roughly as stiff as those in the WT (Figure S4A). Thus, the increased CMT disorganization in the *atktn1* SAM cannot be related to lower stress level caused by stiffer cell walls.

Alternatively, the presence of disorganized CMTs in the *atktn1* SAM could be consistent with a scenario in which *atktn1* cells are less competent to orient their CMTs in response to mechanical stress. To test this hypothesis, we computed the local variability of CMT array anisotropy and the local variability of CMT array orientation for groups of cells comprising a cell and its six closest neighbors in the WT and *atktn1* mutant (Figures 4A and 4B and Extended Experimental Procedures). We reasoned that if the CMT orientation of a given cell depends on the local pattern of stress, the differences in CMT orientations between neighboring cells should be low when cells respond efficiently to stress. Our measurements revealed that the local variability in both CMT anisotropy and CMT orientation was significantly increased in *atktn1* (Figures 4A and 4B), consistent with slower dynamics and a decreased response to the local pattern of stress in *atktn1*. This indirect evidence, together with the previous observation that the least aligned CMTs tend to respond faster to mechanical

stress in the WT (see Figure S11 in Hamant et al., 2008), supports a view in which CMTs are less competent to orient according to the local pattern of stress in the absence of katanin because of a slower microtubule dynamics.

atktn1 Meristematic Cells Are Less Competent to Respond to Changes in Mechanical Stress Pattern

To test more directly whether the response to mechanical stress is decreased in *atktn1*, we next modified the pattern of stress in the SAM and compared the response of the CMTs in the WT and in the *atktn1* mutant.

First, we applied a compressive force of about 0.1N at the base of the meristem with a microvice (Figures 4C–4G). This is predicted to increase mechanical tension in the meristem epidermis, with an increased stress anisotropy parallel to the compressing blades (Figure 4C). As previously observed, this method increased the level of CMT bundling in the WT cells, leading to strongly anisotropic CMTs arrays, with a bias toward the direction parallel to the blades (Figures 4D and 4F) (Hamant et al., 2008). Although the increased CMT bundling could also be observed in *atktn1*, no dominant CMT orientation, i.e., nearly isotropic arrays, could be observed in each cell after compression, consistent with a scenario in which CMTs respond less efficiently to mechanical stress (Figures 4E and 4G).

To confirm this result, we next modified the mechanical stress level using a pharmacological approach (Figures 4H–4L). Isoxaben is a well-known inhibitor of cellulose synthesis (e.g., Desprez et al., 2002). When cellulose synthesis is inhibited, cell walls are predicted to become thinner or at least less resistant to turgor pressure, and thus mechanical stress is supposed to increase (Ryden et al., 2003) (Figure 4H). As previously reported, we observed the formation of CMT bundles in a circumferential pattern matching the predicted stress pattern in the WT after isoxaben treatment (Figures 4I and 4J) (Heisler et al., 2010). In contrast, we were never able to see such a response in the *atktn1* mutant. CMTs remained poorly oriented after isoxaben treatment and rarely made extra bundles, and no clear correlation between meristem shape, predicted stress pattern, and CMT orientation could be drawn (Figures 4K and 4L).

As isoxaben could affect other aspects of the cell physiology, we performed a third test. After single-cell ablation, microtubules will orient in a circumferential pattern around the wound (Hamant et al., 2008; Heisler et al., 2010), which precisely corresponds to predicted stress patterns (Figure 4M). We therefore performed large-scale ablations of the SAM epidermis and followed the responses of the CMTs (Figures 4N–4Q), reasoning that, in these conditions, the modified pattern of stress would still be circumferential, but because of its higher intensity, it would propagate to a larger population of cells. Consistent with this prediction, we observed that the initial ring of cells with circumferential CMTs around the wound expanded to several concentric arrays of cells with circumferential CMTs 23 hr after wounding in the WT (Figures 4N and 4P). In contrast, in the *atktn1 GFP-MBD* line, CMTs became roughly circumferential in the very first cell files around the wound, but the orientation was still random in the cells away from the wound, even 31 hr after the ablation (Figures 4O and 4Q). Based on these images, we could estimate that the level of stress sensed in *atktn1* is about three times lower than in the WT (see Extended
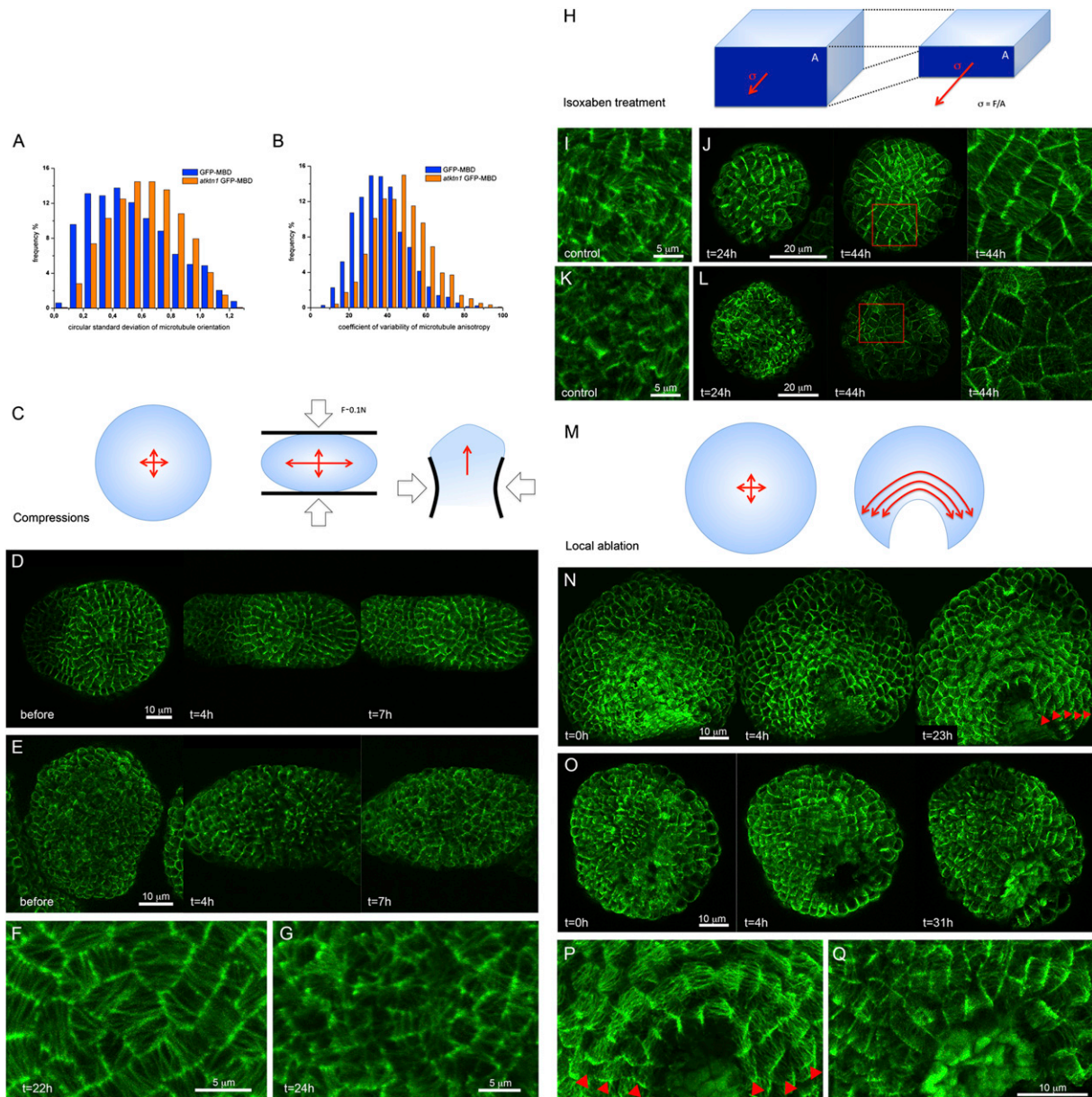
Figure 4. A Decreased Response to Mechanical Stress in *atktn1* Meristematic Cells

(A and B) Local variability of CMT orientation (A) and anisotropy (B) in *GFP-MBD* (blue) and *atktn1 GFP-MBD* (orange). The variability of CMT orientation is represented as distribution of standard deviation for circular data, whereas the variability of CMT anisotropy is represented as a distribution of coefficient of variability (see Extended Experimental Procedures). The local variability was computed for a cell and six of its closest neighbors and assigned for this cell, for the total of n = 2,152 cells (five meristems) of GFP-MBD, and n = 2,128 cells (five meristems) of *atktn1* GFP-MBD. The differences between distributions and means for GFP-MBD and *atktn1* GFP-MBD are statistically significant (Kolmogorov-Smirnov test, p < 0.001; and t test, p < 0.001).

(C–G) After compression, CMTs form parallel bundles (strongly anisotropic arrays) in the WT (D) and bundles with multiple orientations (nearly isotropic) in *atktn1* (E). The phenomenon is pronounced in rare cases when the compression could be maintained for 24 hr, shown for the WT (F) and *atktn1* (G).

(H–L) CMTs at the surface of a representative WT (I) and *atktn1* meristem (K) in the absence of isoxaben (control). After isoxaben treatment, a supracellular circumferential pattern of thick CMT bundles is observed in the WT (J). Such a response is not observed in *atktn1* (L).

(M–Q) Concentric rings of CMTs are observed in the WT after wounding (N), in contrast to a weak response in *atktn1* (O). (P) and (Q) are close-ups from (N) and (O), respectively. Red arrowheads point to supracellular alignments of CMTs in the WT.

Experimental Procedures). Furthermore, and consistent with the CMT response, growth anisotropy was much more marked in the WT than in *atktn1* 48 hr after ablation (Figure S4B).

To further confirm our observations, we performed ablations on isoxaben-treated meristems, reasoning that such a combined protocol should induce higher stress levels. This partially

rescued the response of *atktn1*, indicating that a high level of stress can compensate for a lower response (Figure S4C).

Altogether, these data strongly suggest that katanin provides the cell with the ability to respond efficiently to mechanical stress by increasing microtubule dynamics. Next, we investigated whether this could impact growth homeostasis.

Model: A Mechanical Signal Can Control the Extent of Growth Homeostasis

Previous theoretical work suggests that mechanical stress can lead to uniform growth, and even synchronized mitotic arrest, in animal cells (Aegerter-Wilmsen et al., 2007; Hufnagel et al., 2007; Shraiman, 2005). However, no mechanism had been proposed to mediate such a process. Therefore, we first built a cell-based model of a growing two-dimensional (2D) tissue to examine whether the mechanical response of CMTs can lead to homogeneous growth. As the meristem curvature remains small compared to cell size (except perhaps in boundaries), a 2D model was sufficient to address the differences in behavior between neighboring cells.

In order to investigate the effect of variability in cell growth rate, we sought to implement individual target growth rates in the model directly. Existing formulations were not adapted to this task: turgor-driven models prescribe growth only indirectly as a balance between cell-wall properties and turgor pressure (Corson et al., 2009; Hamant et al., 2008), whereas the continuum approach by Coen et al. (2004) does not allow for cellular resolution. We therefore developed a new vertex model that accounted for anisotropic growth.

The main assumptions of the model are as follows (Figure 5A and Extended Experimental Procedures). (1) We consider that each cell has a target growth rate (the cell-autonomous control of growth), at which it would grow if it were isolated from the tissue. Within the tissue, the cell has an actual growth rate, which may differ from the target growth rate because of neighboring cells. (2) As cell activity is intrinsically variable, we assume that this target growth rate has stochastic variations (fluctuations) across the population of cells. A first important parameter of the model is then the measure of the level of fluctuation of the cell-autonomous control. (3) Growth is symplastic, i.e., cells remain in contact and do not slide against each other. As a consequence, a cell with a larger (or smaller) growth rate than its neighbors pushes (or pulls, respectively) the tissue. In other words, symplastic growth generates mechanical stress. (4) The actual growth of a cell is a result of the target growth rate (which is cell autonomous) and the feedback of mechanical stress (which occurs at the tissue level), assuming that the cell reacts so as to grow less in the orientation of maximal tensile stress. The resistance of a cell to maximal stress is our main hypothesis and follows from our observations on the reorientation of CMTs (Hamant et al., 2008). This resistance is quantified by the second important model parameter, termed feedback strength, which integrates the dynamics of CMTs and of cellulose synthesis. The statistical data of Figure 5 were obtained with 160 runs of a tissue with a hundred cells, for each value of the simulation parameters. In these runs, we did not account for cell division in order to speed up computation and to reduce the number of hypotheses. Implementing cell division actually had little qualitative impact (Figure S5A).

We systematically varied the two main parameters: level of fluctuations and feedback strength. Although we have no empirical data on cell-autonomous fluctuations, our observations imply that the response to stress (feedback strength) is lower in *atktn1* than in WT. Two examples, with and without stress feedback, are shown (Figure 5B). As no qualitative effects are apparent, we constructed a set of measures (see Extended Experimental Procedures) to reveal differences in behavior between neighboring cells when fluctuations are either relatively low or large (Figures 5C–5E). These measures were obtained for each cell and then averaged over the whole tissue and the different simulations. Stress anisotropy ranges from the value 0 for isotropic stress to 1 for unidirectional (anisotropic) stress. Stress variability quantifies the inhomogeneity of stress between a cell and all its neighbors; its value is 0 when the cells in the group have the same value of stress, and it is positive otherwise. These two stress-related quantities vary only slightly with fluctuation level or with feedback strength; only stress variability decreases by a few percent when feedback strength is increased within the investigated range. In this framework, the defective features of CMT patterns in *atktn1*, in particular less ordered CMTs, can be ascribed solely to a lower response to a given stress pattern.

The major conclusions drawn from the model concern the variability of actual growth (Figure 5E). This quantity increases from 0 when the cell and all its neighbors have the same growth rate to larger values when the growth rate is inhomogeneous. First considering the case of a high level of fluctuations, we observed that growth variability initially decreases when the feedback strength is increased, until reaching a minimum. This shows that mechanical feedback can yield more homogenous growth. Surprisingly, when feedback strength was further increased, growth became less homogenous as cells over-react to the stress level. In this first case, it would be tempting to propose that the WT achieves the optimum of homogeneity corresponding to the minimum in growth variability. Unexpectedly, however, we found that for low fluctuation levels, growth variability mainly increased when feedback increased. Therefore, although the orientation of CMTs by stress could help homogenize growth, our model predicts that strong feedback tends in contrast to enhance growth heterogeneity. Based on the questions raised by these conclusions, we next quantified growth variability in WT and *atktn1* SAMs.

Local Variability of Growth Rates Is Decreased in the *atktn1* Mutant

To compare rates of growth in area between neighboring cells, we computed the local variability of growth, defined as the coefficient of variability for groups of cells comprising a cell and its neighbors (Extended Experimental Procedures). In order to consider equivalent cell populations, we excluded boundaries and flower primordia from this analysis. To normalize the results, pooling the cells from different meristems growing at different rates, we plotted the local variability of growth rate assigned to each cell as a function of its own growth rate (Figure 5F). Surprisingly, a rather scattered cloud of points was obtained for the WT, showing that cells with similar growth rates exhibit a very wide range of local variability in growth rates (Figure 5F). This
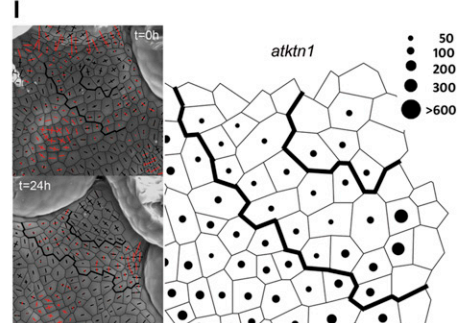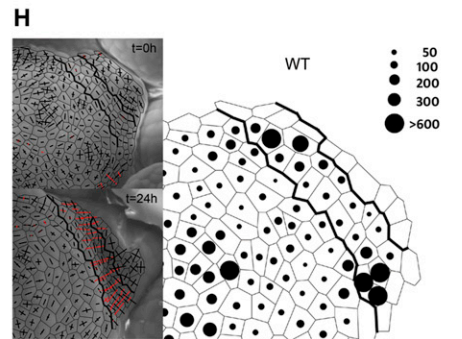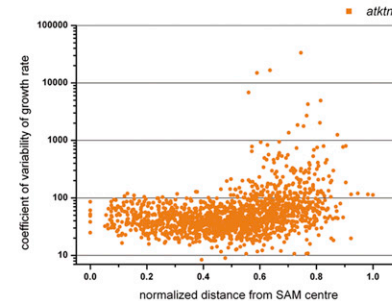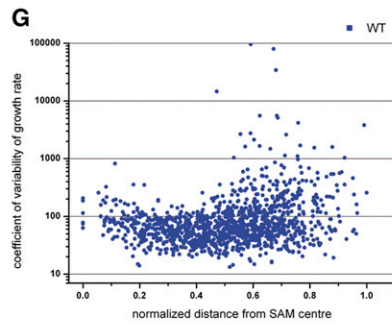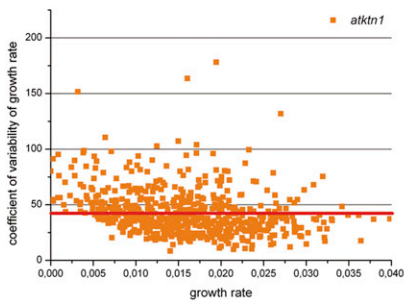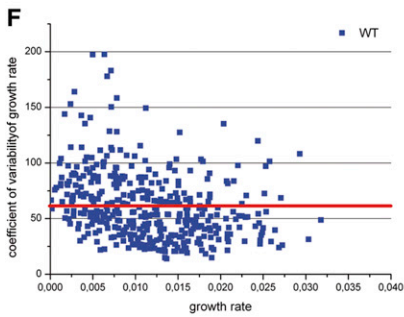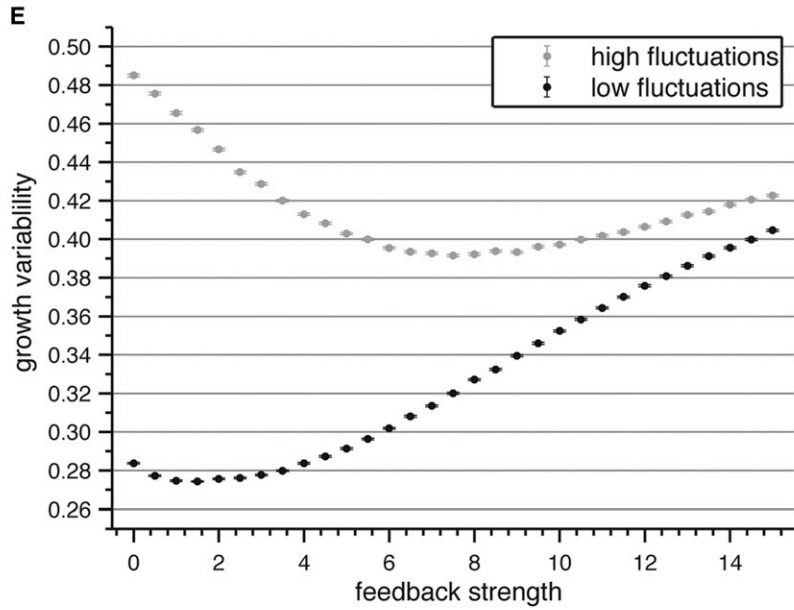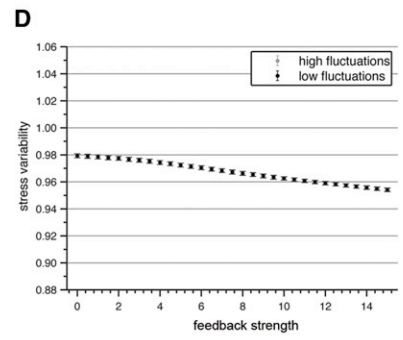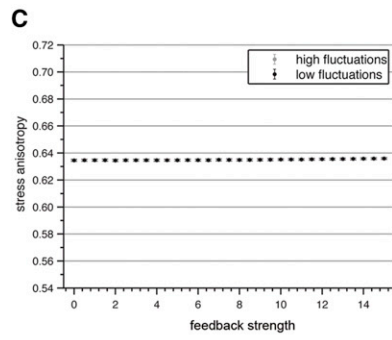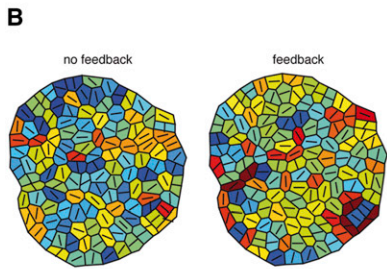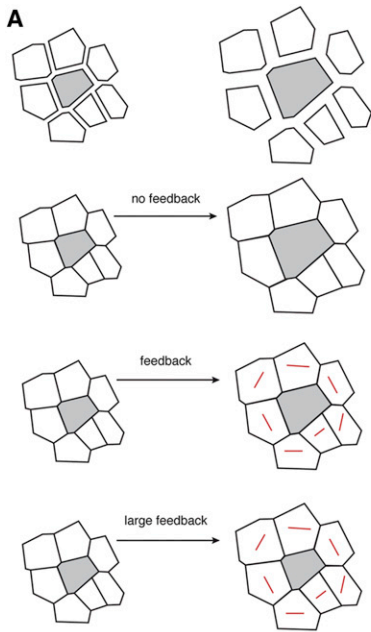
range was much narrower in the *atktn1* mutant (Figure 5F). Furthermore, the mean local variability was significantly lower in the mutant (t test, p < 0.001). Altogether, these results demonstrate that growth among neighboring cells is less heterogeneous in the *atktn1* mutant.

To test this conclusion further, we investigated whether predicted patterns of stress match patterns of growth variability. We first plotted the local variability of growth according to the distance to the center of the meristem, this time including boundaries and primordia in our analysis. Strikingly, local growth variability increased with the distance from the SAM center in both WT and *atktn1* (Figure 5G). To check this result less globally, we plotted the local growth variability on the WT and *atktn1* meristems, focusing on the boundary domain, which exhibits high directional (anisotropic) mechanical stress (Hamant et al., 2008; Kwiatkowska and Dumais, 2003). In both genotypes, growth was more heterogeneous where the boundary was formed (Figures 5H, 5I, and S5B). Growth heterogeneity is thus related to a local pattern of stress. Local growth variability was also still lower in *atktn1* than in WT when boundaries of similar age were compared (Figures 5H, 5I, and S5B). Consistent with growth being less heterogeneous in *atktn1*, the shape of the boundary domain was affected in the *atktn1* mutant (Figure 5I; see also Figure 3E). In particular, whereas the WT exhibited sharp creases next to older primordia, the boundaries at similar plastochron age in the mutant were less sharp, suggesting a delay in boundary formation. We thus propose that mechanical stress promotes growth heterogeneity in the boundary, thus allowing rapid growth rate changes to occur among neighboring cells in this domain and facilitating organ emergence (Figure 6).

DISCUSSION

Lack of Orchestration Leads to More Homogeneity

A central and open question in biology is how cells within a tissue coordinate their growth. Although it is generally thought that growth is locally homogeneous within a tissue, increasing evidence for the stochasticity of cell behavior (Oates, 2011) suggests that neighboring cells might have a growth rate of their own. Here we investigated how growth heterogeneity is controlled and what its function could be in the SAM. More specifically, we provide evidence that katanin-dependent microtubule dynamics increase cell competence to respond to mechanical stress, allowing cells to adapt their growth parameters to those of their neighbors. Although this mechanism could mediate growth homeostasis, we surprisingly found that it enhances growth heterogeneity.

We generated a model in which different scenarios were tested based on the strength of the cell response to mechanical stress. First, our model shows that mechanical forces may decrease growth variability, and it even provides a theoretical optimum of homogeneity corresponding to the minimum of growth variability. These theoretical data are consistent with that of Shraiman and colleagues, suggesting that the synchronous cell-cycle arrest in *Drosophila* imaginal discs is due to tensile stress building up at the periphery of the disc and instantly propagating to the entire tissue to stop growth (Aegerter-Wilmsen et al., 2007; Hufnagel et al., 2007; Shraiman, 2005). We further demonstrate that such a regulation can be mediated by cytoskeletal dynamics. However, our model also shows that the existence of large stress feedback, and most clearly for low fluctuations in growth, can on the contrary increase growth

Figure 5. Impact of Mechanical Feedback on Growth

(A) Graphical representation of the hypothesis implemented in the model. Each cell is assigned a random target growth rate that it would achieve if isolated from its neighbors (here the gray cell has a large target growth rate). This randomness quantifies the level of imposed fluctuations across the cell population. Within a tissue, a cell with a larger growth rate pushes on its neighbors, inducing mechanical stress. When feedback of stress on growth is implemented, cells restrain growth in the direction of the red lines, thus reducing the actual growth of the gray cell.

(B) Graphical output of the computer simulations with or without mechanical stress feedback. The vertex model accounts for random target growth per cell and mechanical interactions between cells. Each line corresponds to the maximal stress direction within a cell, whereas the level of mechanical stress is color-coded (from blue to red with increasing stress).

(C and D) Stress anisotropy and stress variability when stress feedback strength changes. Stress anisotropy varies between 0 (isotropic stress) and 1 (highly anisotropic stress). Stress variability measures the difference in stress level between a cell and its neighbors and takes the value 0 when all cells have the same level. These two stress-related quantities are only slightly affected by feedback strength or by fluctuation level. Error bars are SEM.

(E) Growth variability when stress feedback strength changes. Growth variability measures the difference in growth rate between a cell and its neighbors and takes the value 0 when all cells grow at the same rate. If target growth experiences high fluctuations, the response to mechanical stress is first predicted to render growth among neighboring cells more homogenous and as stress increases, growth variability then increases. If target growth is more stable (low fluctuations), the response to mechanical stress is predicted to increase the variability of growth among neighboring cells. Error bars are SEM.

(F) Coefficient of variability (local variability representation) of growth rates plotted against the growth rate for the individual SAM cells (excluding boundaries and primordia) of WT (blue) and *atktn1* (orange). To be consistent with the modeling protocol, the growth rates were computed by polygon approach (see Extended Experimental Procedures). Coefficient of variability was computed for a cell and all its contacting neighbors and assigned to this cell, for the total of n = 410 cells (six meristems) of WT and n = 607 cells (six meristems) of *atktn1*. The horizontal red lines indicate the mean coefficient of variability. The means for WT and *atktn1* are significantly different (t test, p < 0.001).

(G) Coefficient of variability of growth rates plotted against the distance to the center of the SAM in the WT (blue) and *atktn1* (orange). Coefficient of variability was computed for a cell and six of its closest neighbors and assigned to this cell, for the total of n = 1,223 cells (six meristems) of WT and n = 1,587 cells (six meristems) of *atktn1*. Cells from the SAM and adjacent boundaries and the youngest primordia were considered. Because of high coefficient variation, the y axis is in logarithmic scale. The distance from the SAM center is normalized.

(H and I) Spatial distribution of coefficient of variability (in percent) of growth rates in the boundaries of primordia exhibiting similar plastochron age in the WT (H) and *atktn1* (I). The size of the disc increases with the coefficient value. Scanning electron micrographs with overlaid principal curvature directions for both genotypes are included. Regions that will give rise to boundaries (creases with a negative curvature in meridional direction) during the next 24 hr are delineated with thick lines. Mean ± SEM coefficient of variability in the boundary is 608% ± 271% in WT (n = 19 cells) and 36% ± 7% in *atktn1* (n = 19 cells).
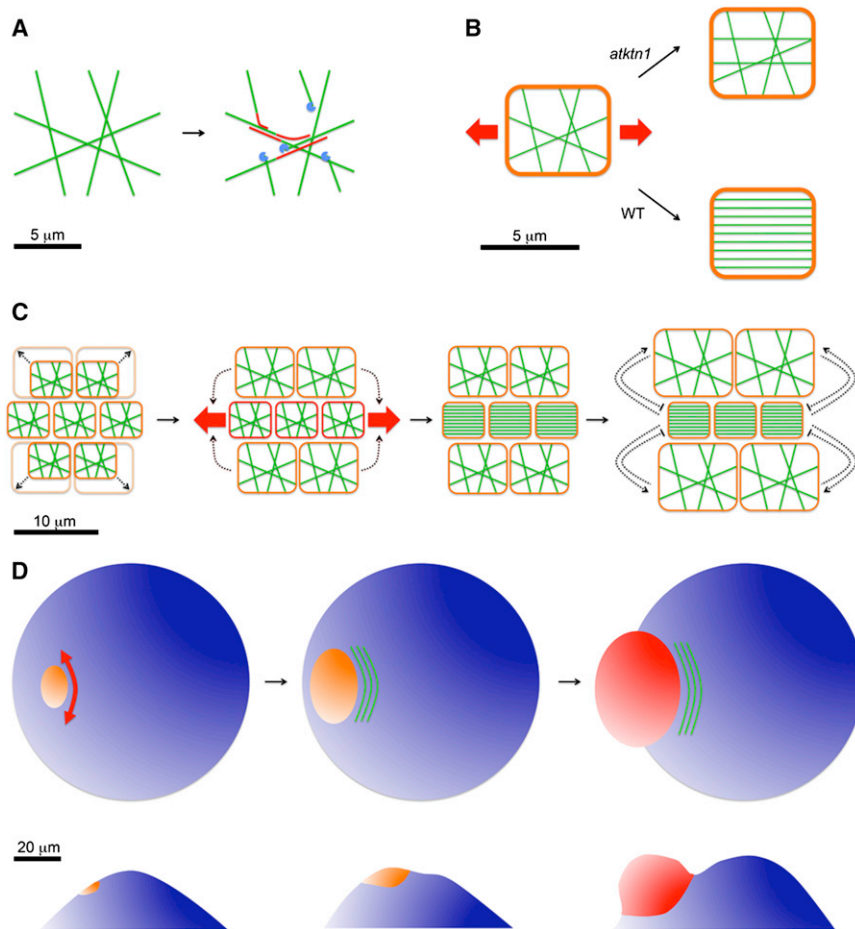
Figure 6. From Microtubule Severing to Morphogenesis: Katanin Function in a Multi-scale Perspective

(A) The molecular level: Katanin (blue) severs microtubules and enhances their encounters and bundling (red).

(B) The cellular level: Microtubule encounters enhance CMT self-organization in parallel arrays, which is reduced in the *atktn1* mutant. Parallel CMTs drive growth anisotropy.

(C) The tissue level: Differential growth modifies the pattern of mechanical stress (red arrows), which in turn controls the CMT orientation and thus growth anisotropy. This in turn enhances the gradient in growth rate, further amplifying differential growth pattern in a feedback loop.

(D) The organ level: Increased anisotropy (CMT orientation in green) and increased differential growth next to an emerging organ (increasing growth rate is color-coded from orange to red) in the SAM (blue) promote tissue folding and organ emergence. Top views (top) and side views (bottom) are presented.

on stress response and growth, can account for all of the morphogenetic defects in *atktn1*, it seems more parsimonious to restrict our conclusion to the contribution of CMTs in controlling shape in *atktn1*.

The increased bumpiness of the SAM surface in *atktn1* may be associated with the random orientation of CMTs, as demonstrated by the presence of oblique cell division planes, which may locally unleash growth in the anticlinal direction. On a larger scale, we might ascribe the presence of a depression in the CZ (i.e., a ring of outgrowth in the PZ) to the decreased growth anisotropy in the PZ of the *atktn1* mutant. This also suggests that the SAM exhibits a crater-like shape by default, and that the balance between growth rate and growth anisotropy is tightly regulated to prevent organogenesis and maintain a dome shape. To some extent, this finding echoes the work by Nath et al. (2003) suggesting that plant leaves are ruffled by default and that growth parameters must be tightly regulated to maintain a flat shape. In this respect, it would be interesting to expand our analysis to the vegetative SAM, which exhibits a rather flat shape in the WT.

In animals, although growth rate (mainly by cell proliferation) was classically seen as the main contributor to shape changes in young tissues, the balance with growth anisotropy is also emerging as a major contributing factor determining shape. As an example, the outgrowth of the limb in tetrapods has long been proposed to depend on an increased growth rate at the emerging limb periphery (Towers and Tickle, 2009). Nevertheless, Boehm and collaborators (Boehm et al., 2010) generated a 3D map of proliferation rates in the developing limb bud together with a finite element-based model showing that the gradient in proliferation rate is not sufficient to explain the limb

variability. This last scenario is validated by our growth measurements, indicating that mechanical stress exerts a positive feedback on differential growth. This also suggests that, despite the existence of a theoretical optimum where growth is homogeneous, growth in planta is suboptimal, thus maintaining the ability to generate and amplify differential growth. This is probably relevant during organogenesis in the SAM: as the organ starts to emerge thanks to an initial gradient in growth rates, suboptimal growth regulation allows the cells to over-react to mechanical stress, further enhancing this gradient. Competence to react to stochastic growth would thus act as a template to induce sharp growth-rate gradients.

The Balance between Growth Rate and Growth Anisotropy Explains the Robustness of Shapes

In addition to tissue folding delays in the boundary domain in the *atktn1* SAM, major morphogenetic defects were observed. Importantly, we cannot exclude the possibility that other downstream biochemical signals may contribute to the aberrant SAM shape in *atktn1*. In this respect, it would be interesting to investigate whether morphogen gradients are modified by a decreased response to mechanical stress. However, the only known biochemical activity of katanin is microtubule severing. Because the decreased CMT dynamics, and their direct impact

shape and suggesting that an active anisotropic cell behavior has a major role in shaping the limb.

Toward a Universal Role of Cytoskeletal Regulators in the Mechanical Control of Growth Coordination

Although the relative contribution of mechanical and biochemical signals in the *katanin* loss-of-function phenotype remains to be determined, our work puts forward the role for katanin in providing competence to respond efficiently to mechanical stress. In animal systems, several cytoskeletal proteins have also been shown to contribute to cellular response to mechanical signals. However, in contrast to plants, these proteins are largely associated with the F-actin cytoskeleton. In particular, the acto-myosin network reorganizes in response to mechanical forces, and this has a crucial impact on tissue morphogenesis (Lecuit and Lenne, 2007). Mechanical forces can also change the conformation of alpha-catenins, allowing them to recruit vinculin, an actin-binding protein, at the site of cell adhesion (Yonemura et al., 2010). At this stage, and by analogy with our data on katanin and the dominant role of CMTs in shaping plant tissues, we can thus predict that F-actin-severing proteins, like cofilin or gelsolin, or actomyosin regulators, like formins or myosin kinases, might control the competence of animal cells to respond to mechanical stress. In this framework, the role of these regulators on growth and morphogenesis could be addressed by taking into account their putative role in growth coordination.

Stochasticity as a Source of Instructional Signals

If developmental biology is concerned with the question of how reproducible shapes can emerge from the behavior of individual cells, our study provides a mechanism through which the variability among individual cells contributes to the robustness of morphogenesis. This counterintuitive conclusion highlights the contribution of stochasticity in development. Stochasticity is in fact emerging as an essential factor in many biological processes (Oates, 2011). For instance, the observation that transcription levels are noisy by default has been associated with fundamental biological responses, such as incomplete penetrance (Raj et al., 2010). In the frame of developmental biology, such transcriptional noise may impact the precision of spatiotemporal patterns (Oates, 2011). Beyond transcription, numerous intracellular components have been shown to exhibit noisy behavior, and this is even thought to be a key factor in evolution (Eldar and Elowitz, 2010). The development of quantitative approaches coupled with computer simulations is likely to decipher the many contributions of stochasticity in development in the near future.

EXPERIMENTAL PROCEDURES

Plant Material and Growth Conditions

To analyze the defects in the *atktn1* mutant, we used the *bot1-7* katanin allele that was previously isolated by Bichet and collaborators (Bichet et al., 2001). The *bot1-7* allele bears a deletion of 19 bp from position 31 of the katanin cDNA, leading to a predicted highly truncated protein containing the 10 first amino acids on the katanin, followed by 6 new amino acids (frameshift). The growth analysis was performed on shoots in a defined developmental window, i.e., between the appearance of the first flower to the appearance of first silique (stages 13 to 17, as defined by Smyth et al., 1990).

Confocal Laser-Scanning Microscopy and Chemical Treatments

For most experiments, meristems were prepared from plants grown in a phytotron and microscopy was conducted as described previously (Hamant et al., 2008; Heisler et al., 2010) (see Extended Experimental Procedures for details). All experiments were repeated at least five times, with comparable results.

Replica Method and Scanning Electron Microscopy

Sequences of replicas were taken from individual shoot apices, as described previously (Dumais and Kwiatkowska, 2002; Williams and Green, 1988). Sequences of replicas were taken from seven apices of WT (four grown in Lyon, three grown in Katowice) and seven *atktn1* (four and three, respectively) shoot apices. Two replicas were taken from each individual apex at 24 hr intervals (see Extended Experimental Procedures for details).

Image Analysis and Model

In order to quantify the main orientation of MTs in a cell and measure how well they are aligned, we employed the concept of nematic tensor from the physics of liquid crystals (Gennes and Prost, 1993). Basically, the direction of the gradient of the intensity of the GFP signal gives the local direction normal to CMTs. A proper normalization ensures independence of variations in fluorescence level. Appropriate averaging over a cell yields an angle, corresponding to the main orientation of CMTs in this cell, and a number, termed anisotropy of CMT arrays, that measures how well CMTs are organized in parallel arrays. More precisely, the anisotropy of arrays ranges from 0 when the orientation of bundles in the cell is random to a maximum theoretical value of 1 when all CMTs bundles are oriented in the same direction (see Extended Experimental Procedures for details). To measure growth rate in area, growth anisotropy, and variability of growth, we adapted previously published tools written in Matlab (Dumais and Kwiatkowska, 2002; Routier-Kierzkowska and Kwiatkowska, 2008) (see Extended Experimental Procedures for details). The impact of neighboring cells and associated mechanical stress on growth was simulated in a vertex-based model. We incorporated in this model the known response of CMTs to mechanical stress and their impact on growth anisotropy (see Extended Experimental Procedures for details).

REFERENCES

Aegerter-Wilmsen, T., Aegerter, C.M., Hafen, E., and Basler, K. (2007). Model for the regulation of size in the wing imaginal disc of Drosophila. Mech. Dev. *124*, 318–326.

Allard, J.F., Wasteneys, G.O., and Cytrynbaum, E.N. (2010). Mechanisms of self-organization of cortical microtubules in plants revealed by computational simulations. Mol. Biol. Cell *21*, 278–286.

Bichet, A., Desnos, T., Turner, S., Grandjean, O., and Höfte, H. (2001). BOTERO1 is required for normal orientation of cortical microtubules and anisotropic cell expansion in Arabidopsis. Plant J. *25*, 137–148.

Boehm, B., Westerberg, H., Lesnicar-Pucko, G., Raja, S., Rautschka, M., Cotterell, J., Swoger, J., and Sharpe, J. (2010). The role of spatially controlled cell proliferation in limb bud morphogenesis. PLoS Biol. *8*, e1000420.

Burk, D.H., and Ye, Z.H. (2002). Alteration of oriented deposition of cellulose microfibrils by mutation of a katanin-like microtubule-severing protein. Plant Cell *14*, 2145–2160.

Burk, D.H., Liu, B., Zhong, R., Morrison, W.H., and Ye, Z.H. (2001). A katanin-like protein regulates normal cell wall biosynthesis and cell elongation. Plant Cell *13*, 807–827.

Cleary, A.L., and Hardham, A.R. (1993). Pressure induced reorientation of cortical microtubules in epidermal cells of Lolium rigidum leaves. Plant Cell Physiol. *34*, 1003–1008.

Coen, E., Rolland-Lagan, A.G., Matthews, M., Bangham, J.A., and Prusinkie-wicz, P. (2004). The genetics of geometry. Proc. Natl. Acad. Sci. USA *101*, 4728–4735.

Corson, F., Hamant, O., Bohn, S., Traas, J., Boudaoud, A., and Couder, Y. (2009). Turning a plant tissue into a living cell froth through isotropic growth. Proc. Natl. Acad. Sci. USA *106*, 8453–8458.

Desprez, T., Vernhettes, S., Fagard, M., Refrégier, G., Desnos, T., Aletti, E., Py, N., Pelletier, S., and Höfte, H. (2002). Resistance against herbicide isoxaben and cellulose deficiency caused by distinct mutations in same cellulose synthase isoform CESA6. Plant Physiol. *128*, 482–490.

Dixit, R., and Cyr, R. (2004). The cortical microtubule array: from dynamics to organization. Plant Cell *16*, 2546–2552.

Dumais, J., and Kwiatkowska, D. (2002). Analysis of surface growth in shoot apices. Plant J. *31*, 229–241.

Eldar, A., and Elowitz, M.B. (2010). Functional roles for noise in genetic circuits. Nature *467*, 167–173.

Farge, E. (2003). Mechanical induction of Twist in the Drosophila foregut/stomodeal primordium. Curr. Biol. *13*, 1365–1377.

Fink, J., Carpi, N., Betz, T., Bétard, A., Chebah, M., Azioune, A., Bornens, M., Sykes, C., Fetler, L., Cuvelier, D., and Piel, M. (2011). External forces control mitotic spindle positioning. Nat. Cell Biol. *13*, 771–778.

Gennes, P.G.d., and Prost, J. (1993). The Physics of Liquid Crystals, 2nd edn (Oxford, UK: Oxford University Press).

Grashoff, C., Hoffman, B.D., Brenner, M.D., Zhou, R., Parsons, M., Yang, M.T., McLean, M.A., Sligar, S.G., Chen, C.S., Ha, T., and Schwartz, M.A. (2010). Measuring mechanical tension across vinculin reveals regulation of focal adhesion dynamics. Nature *466*, 263–266.

Green, P.B., and King, A. (1966). A mechanism for the origin of specifically oriented textures in development with special reference to Nitella wall structure. Aust. J. Biol. Sci. *19*, 421–437.

Hamant, O., Heisler, M.G., Jönsson, H., Krupinski, P., Uyttewaal, M., Bokov, P., Corson, F., Sahlin, P., Boudaoud, A., Meyerowitz, E.M., et al. (2008). Developmental patterning by mechanical signals in Arabidopsis. Science *322*, 1650–1655.

Heisler, M.G., Hamant, O., Krupinski, P., Uyttewaal, M., Ohno, C., Jönsson, H., Traas, J., and Meyerowitz, E.M. (2010). Alignment between PIN1 polarity and microtubule orientation in the shoot apical meristem reveals a tight coupling between morphogenesis and auxin transport. PLoS Biol. *8*, e1000516.

Hufnagel, L., Teleman, A.A., Rouault, H., Cohen, S.M., and Shraiman, B.I. (2007). On the mechanism of wing size determination in fly development. Proc. Natl. Acad. Sci. USA *104*, 3835–3840.

Jaeger, J., Irons, D., and Monk, N. (2008). Regulative feedback in pattern formation: towards a general relativistic theory of positional information. Development *135*, 3175–3183.

Jarvis, M.C., Briggs, S.P.H., and Knox, J.P. (2003). Intercellular adhesion and cell separation in plants. Plant Cell Environ. *26*, 977–989.

Kwiatkowska, D., and Dumais, J. (2003). Growth and morphogenesis at the vegetative shoot apex of Anagallis arvensis L. J. Exp. Bot. *54*, 1585–1595.

Landsberg, K.P., Farhadifar, R., Ranft, J., Umetsu, D., Widmann, T.J., Bittig, T., Said, A., Jülicher, F., and Dahmann, C. (2009). Increased cell bond tension governs cell sorting at the Drosophila anteroposterior compartment boundary. Curr. Biol. *19*, 1950–1955.

Lecuit, T., and Lenne, P.F. (2007). Cell surface mechanics and the control of cell shape, tissue patterns and morphogenesis. Nat. Rev. Mol. Cell Biol. *8*, 633–644.

Mirabet, V., Das, P., Boudaoud, A., and Hamant, O. (2011). The role of mechanical forces in plant morphogenesis. Annu. Rev. Plant Biol. *62*, 365–385.

Monshausen, G.B., and Gilroy, S. (2009). Feeling green: mechanosensing in plants. Trends Cell Biol. *19*, 228–235.

Nakamura, M., Ehrhardt, D.W., and Hashimoto, T. (2010). Microtubule and katanin-dependent dynamics of microtubule nucleation complexes in the acentrosomal Arabidopsis cortical array. Nat. Cell Biol. *12*, 1064–1070.

Nath, U., Crawford, B.C., Carpenter, R., and Coen, E. (2003). Genetic control of surface curvature. Science *299*, 1404–1407.

Oates, A.C. (2011). What's all the noise about developmental stochasticity? Development *138*, 601–607.

Paredez, A.R., Somerville, C.R., and Ehrhardt, D.W. (2006). Visualization of cellulose synthase demonstrates functional association with microtubules. Science *312*, 1491–1495.

Peaucelle, A., Braybrook, S.A., Le Guillou, L., Bron, E., Kuhlemeier, C., and Höfte, H. (2011). Pectin-induced changes in cell wall mechanics underlie organ initiation in Arabidopsis. Curr. Biol. *21*, 1720–1726.

Raj, A., Rifkin, S.A., Andersen, E., and van Oudenaarden, A. (2010). Variability in gene expression underlies incomplete penetrance. Nature *463*, 913–918.

Routier-Kierzkowska, A.-L., and Kwiatkowska, D. (2008). New stereoscopic reconstruction protocol for scanning electron microscope images and its application to in vivo replicas of the shoot apical meristem. Funct. Plant Biol. *35*, 1034–1046.

Ryden, P., Sugimoto-Shirasu, K., Smith, A.C., Findlay, K., Reiter, W.D., and McCann, M.C. (2003). Tensile properties of Arabidopsis cell walls depend on both a xyloglucan cross-linked microfibrillar network and rhamnogalacturonan II-borate complexes. Plant Physiol. *132*, 1033–1040.

Sakaguchi, S., Hogetsu, T., and Hara, N. (1988). Arrangement of cortical microtubules at the surface of the shoot apex in Vinca major L.: observations by immunofluorescence microscopy. The Botanical Magazine,Tokyo *101*, 497–507.

Shaw, S.L., Kamyar, R., and Ehrhardt, D.W. (2003). Sustained microtubule treadmilling in Arabidopsis cortical arrays. Science *300*, 1715–1718.

Shraiman, B.I. (2005). Mechanical feedback as a possible regulator of tissue growth. Proc. Natl. Acad. Sci. USA *102*, 3318–3323.

Smyth, D.R., Bowman, J.L., and Meyerowitz, E.M. (1990). Early flower development in *Arabidopsis*. Plant Cell *2*, 755–767.

Stoppin-Mellet, V., Gaillard, J., and Vantard, M. (2006). Katanin's severing activity favors bundling of cortical microtubules in plants. Plant J. *46*, 1009–1017.

Théry, M., Jiménez-Dalmaroni, A., Racine, V., Bornens, M., and Jülicher, F. (2007). Experimental and theoretical study of mitotic spindle orientation. Nature *447*, 493–496.

Towers, M., and Tickle, C. (2009). Growing models of vertebrate limb development. Development *136*, 179–190.

Vogel, V., and Sheetz, M. (2006). Local force and geometry sensing regulate cell functions. Nat. Rev. Mol. Cell Biol. *7*, 265–275.

Wartlick, O., Kicheva, A., and González-Gaitán, M. (2009). Morphogen gradient formation. Cold Spring Harb. Perspect. Biol. *1*, a001255.

Wasteneys, G.O., and Ambrose, J.C. (2009). Spatial organization of plant cortical microtubules: close encounters of the 2D kind. Trends Cell Biol. *19*, 62–71.

Williams, M.H., and Green, P.B. (1988). Sequential scanning electron microscopy of a growing plant meristem. Protoplasma *147*, 77–79.

Williams, M.H., Vesk, M., and Mullins, M.G. (1987). Tissue preparation for scanning electron microscopy of fruit surfaces: Comparison of fresh and cryopreserved specimens and replicas of banana peel. Micron and Microscopica Acta *18*, 27–31.

Williamson, R.E. (1990). Alignment of cortical microtubules by anisotropic wall stresses. Aust. J. Plant Physiol. *17*, 601–613.

Wolpert, L. (1969). Positional information and the spatial pattern of cellular differentiation. J. Theor. Biol. *25*, 1–47.

Wymer, C.L., Wymer, S.A., Cosgrove, D.J., and Cyr, R.J. (1996). Plant cell growth responds to external forces and the response requires intact microtubules. Plant Physiol. *110*, 425–430.

Yonemura, S., Wada, Y., Watanabe, T., Nagafuchi, A., and Shibata, M. (2010). alpha-Catenin as a tension transducer that induces adherens junction development. Nat. Cell Biol. *12*, 533–542.

Supplemental Information

EXTENDED EXPERIMENTAL PROCEDURES

Plant Material and Growth Conditions

To analyze the defects in the *atktn1* mutant, we used the *bot1-7* katanin allele that was previously isolated by Bichet and collaborators (Bichet et al., 2001). Seeds were kindly provided by Herman Höfte (INRA Versailles). The *bot1-7* allele bears a deletion of 19 bp from position 31 of the katanin cDNA, leading to a predicted highly truncated protein containing the 10 first amino acids on the katanin, followed by 6 new amino-acids (frameshift). Seeds of *Arabidopsis thaliana*, ecotypes *Wassilewskija* (*WS*) were provided by the *Arabidopsis* Biological Resource Centre (Ohio State University, Columbus, USA). The GFP-MBD line was a kind gift from Martine Pastuglia. Alcohol inducible line expressing the *GFP* under the control of the *CLAVATA3* promoter were provided by Patrick Laufs (Deveaux et al., 2003). Experiments were performed on plants grown in phytotrons located in Lyon (France) and Katowice (Poland). In Lyon plants were initially grown in short-day conditions (8 hr/16 hr light/dark period) for 2 weeks and in long-day conditions (16 hr/8 hr light/dark period) afterwards, while in Katowice plants were grown in long-day conditions only. The growth analysis was performed on inflorescence shoots at similar stage of development. As the wild-type and the *atktn1* mutant differ in size, the stem length is not a good marker of developmental stage. The growth analysis was thus performed on shoots in a defined developmental window, i.e., between the appearance of the first flower to the appearance of first silique (stages 13 to 17, as defined by Smyth et al., 1990).

Confocal Laser-Scanning Microscopy and Chemical Treatments

For most experiments, meristems were prepared from plants grown in a phytotron, as described in Fernandez et al. (2010). For isoxaben treatments, NPA grown in vitro seedlings were used to image the meristem, as described in (Heisler et al., 2010). Wounding experiments were realized on meristems from both NPA grown in vitro seedlings and phytotron grown plants, and gave comparable results in both cases. Microscopy was conducted as described previously (Hamant et al., 2008). Projections of the meristem surface were generated using the Merryproj software (de Reuille et al., 2005). All experiments were repeated at least five times, with comparable results.

Replica Method and Scanning Electron Microscopy

Sequences of replicas were taken from individual shoot apices, as described previously (Dumais and Kwiatkowska, 2002; Williams and Green, 1988). The molds (Take 1, Kerr impression materials) were used to obtain epoxy resin casts (Devcon 2 ton epoxy) that were sputter-coated and observed in the scanning electron microscopy (Philips XL 30 TMP ESEN). Sequences of replicas were taken from seven apices of WT (four grown in Lyon, three grown in Katowice) and seven *atktn1* (four and three, respectively) shoot apices. Two replicas were taken from each individual apex at 24 hr interval.

Quantitative Analysis of Microtubule Arrays

In order to quantify the main orientation of MTs in a cell and measure how well they are aligned, we employed the concept of nematic tensor from the physics of liquid crystals (Gennes and Prost, 1993). Let $I(x,y)$ be the intensity level of fluorescence in the image, as a function of the coordinates (x,y). The unit vector $\mathbf{t} = (\mathbf{t}_x, \mathbf{t}_y) = (\partial I/\partial y, -\partial I/\partial x)/\sqrt{(\partial I/\partial x)^2 + (\partial I/\partial y)^2}$ is the tangent to the lines of constant intensity (it defines the local orientation of MTs in a *GFP-MBD* image). The local nematic tensor $\mathbf{n} = \mathbf{t} \otimes \mathbf{t}$ is the 2x2 symmetric matrix of components $\mathbf{n}_{x,x} = \mathbf{t}_x^2$, $\mathbf{n}_{x,y} = \mathbf{n}_{y,x} = \mathbf{t}_x \mathbf{t}_y$, $\mathbf{n}_{y,y} = \mathbf{t}_y^2$. The nematic tensor of the cell is the average <$\mathbf{n}$> of the local tensor over the region of interest. Let $n_1 > n_2$ be the eigenvalues of <$\mathbf{n}$>. The eigenvector $\mathbf{e}_1$ of <$\mathbf{n}$> corresponding to the eigenvalue n_1 defines the main orientation of CMTs in the region of interest, while $q = (n_1 - n_2)/(n_1 + n_2) = n_1 - n_2$ defines the anisotropy of the CMTs arrays ($n_1 + n_2 = 1$ because $\mathbf{t}$ is a unit vector). Indeed, it can be shown mathematically that if all lines of constant intensity are parallel, then $q = 1$ and $\mathbf{e}_1$ is parallel to these lines, whereas if the lines of constant intensity are randomly oriented then $q = 0$ and the orientation is ill-defined. We built an ImageJ MT plugin that implements $\mathbf{e}_1$ and q for a region selected with the polygon tool. In order to avoid numerical errors originating in regions of flat intensity, the local nematic tensor is set to zero whenever the gradient of $I(x,y)$ is smaller than 2/255.

Knowing the average orientation of CMTs and array anisotropy for each meristem cell we quantify the local variability of these variables for groups of cells comprising a given cell and its six closest neighbors. Since the orientation is a directional variable we employ statistics for circular data and compute local variability as a circular standard deviation (Berens, 2009). In the case of the anisotropy (a scalar) we use linear statistics and compute the local variability as a coefficient of variability (i.e., the ratio of standard deviation and mean, in percent, Zar, 1999).

Quantitative Analysis of Curvature and Growth

Stereopairs of scanning electron microscopy images of epoxy resin replicas were used for the stereoscopic reconstruction of the shoot apex surface, based on Routier-Kierzkowska and Kwiatkowska (Routier-Kierzkowska and Kwiatkowska, 2008) protocol (Figure 2A). From the reconstructed meristem surfaces 3D coordinates of vertices, i.e., contact points between anticlinal walls of adjacent cells, were extracted (Figure 2A') and used for further computations. First, surface area was computed for all the L1 meristem cells as the sum of surface areas of all the triangles defined by two adjacent cell vertices and the cell centroid. Next, principal

curvature directions at the cell centroid, i.e., the directions in which the normal curves lying on the surface attain maximal or minimal value, were computed as described previously (Dumais and Kwiatkowska, 2002). Note that such computed curvature directions do not refer to the outer periclinal cell walls, but to the surfaces approximating positions of vertices belonging to a given cell and its closest (contacting) neighbors. The local curvature quantification was used to define meristem boundaries as previously described (Kwiatkowska, 2004; Kwiatkowska and Dumais, 2003).

On the basis of anticlinal cell-wall pattern visible on the meristem surface, the same vertices were recognized in successive replicas and used as landmarks to compute growth variables (Dumais and Kwiatkowska, 2002) for the total of 12 meristems (three from each genotype, both from plants grown in Lyon and in Katowice). Previously described protocols (Dumais and Kwiatkowska, 2002) were employed to compute principal directions of growth rate, growth rate anisotropy, and growth rate in area for each meristem cell (Figure 2A"). Briefly, principal directions of growth rate, i.e., direction in which growth rate attains minimal and maximal values (the rates $rate_{min}$ and $rate_{max}$, respectively), were assessed first for each vertex from the deformation of a triangle defined by the vertex "natural" neighbors (with which it shares a common wall) taking place during growth. The principal directions of growth rate of a cell were then computed on the basis of principal directions of all its vertices (Figure 2A" upper row). The anisotropy of cell growth was computed as absolute value of $(rate_{max} - rate_{min}) / (rate_{min} + rate_{max})$. Growth rate in area of cells was computed either as $rate_{min} + rate_{max}$ (vertex approach) or as $\ln(A'/A)/\Delta t$, where A and A' are the surface area of the cell (or the cell progeny) before and after growth, respectively, and Δt is the time interval between the replica taking (polygon approach, Figure 2A", lower row).

In order to quantify the local variability of growth, coefficient of variability (the ratio of standard deviation and mean, in percent, Zar, 1999) was computed for groups of cells comprising a cell and all its contacting neighbors or a cell and its six closest neighbors.

All codes used for this analysis have been written in Matlab (The Mathworks, Natick, MA, USA). Descriptive statistics, statistical tests, and plots have been performed with the aid of Statistics Toolbox of Matlab (The Mathworks), Statistica (StatSoft, USA) and Origin (OriginLab Corporation, USA).

Results of growth analysis, including growth anisotropy and local variability, performed on plants from Lyon and Katowice laboratories were very similar. While the curvature analysis has shown that the depression in the center of *atktn1* SAM is more apparent in the case of plants grown in Lyon (Figures 3C and S3), the differences between mean values of maximal and minimal curvatures in *atktn1* and WT SAMs were nevertheless significant for the plants grown in Katowice. Generally, the growth rate and cell division frequency were higher in case of plants from Lyon, which probably leads to more apparent *atknt1* phenotype, with regards to SAM geometry.

AFM Measurements

The protocol we used is described in Peaucelle et al. (2011). Briefly, dissected meristems were plasmolyzed in 10% (0.55 M) mannitol prior to measurement using a Nanowizard I AFM from JPK. A lever of stiffness 56N/m was used, equipped with a glass bead of 5μm used for indentation. An approach and retract period of 0.3 s with no delay was used and a constant maximum force was imposed; this value was determined for each experiment, to obtain a maximum deformation at all points of the sample of about 500 nm (10% deformation of a meristematic L1 cell in *Arabidopsis*).

Estimation of Elastic Moduli from Compression Experiments

We used the compression experiments to estimate the elastic moduli of WT and *atktn1* in which two blade press transversely on the stems of NPA-grown plants, very close to the apex. We monitored the optical transverse section of the stem located at the level of the blades top (about 20 μm below the summit) and measured how the contour of this section is deformed following compression, yielding the indentation distance *d*.

The applied force *F* was deduced from the bending of the more flexible blade, and the correspondence between blade bending and applied force was calibrated using a precision scale; the force generally reached a maximum value of 0.1N. The blades have a thickness of 300 μm, are smoothed at the edge, so that they can be locally (close to the contact with the shoot) considered as cylinders of radius *r* = 150 μm.

We assumed the stem to be in the shape of a cylinder of radius *R* (measured from optical sections), which varied in the range 25 to 50 μm according to samples. We estimated the elastic modulus *E* that the stem would have if it were a continuous medium, which can be viewed as an effective elastic modulus. We assumed the Poisson ratio to be 1/2 as the material is mostly water and so is incompressible.

We followed the formulae given in Johnson (1985). As long as the ratio between the radii of the two cylinders is smaller than 10, as is the case here, a good approximation to the effective elastic modulus is

$$E = \frac{9F}{16\,(R\,r)^{1/4}d^{3/2}}.$$

This equation allows us to compare phenotypes, but given the simplification of the geometry, the absolute values of elastic moduli are only indicative.

Four compressed apices from WT and 4 from *atktn1* were analyzed. The values of elastic moduli were found as 204 ± 91 MPa (mean ± SD) and 218 ± 105 MPa. Consequently, the two phenotypes are indistinguishable with respect to mechanical properties.

Estimation of Sensitivity to Stress from Ablations

Let S be the average stress field in the epidermis. Following Landau and Lifshits (1970) and Mora and Boudaoud (2006), the nonisotropic part of the stress field in a 2D medium (corresponding to the epidermis), caused by an ablation of radius R, decreases with the distance from the center r, as $S(R/r)^2$. Given that the mechanical properties of WT and *atktn1* are close, we assume that the stress level S is the same in the two backgrounds. In experiments, the radius of ablations is about 2 cells, the radius at which WT cells respond is 5 cells (3 cell files in which microtubules respond) while the radius at which *atktn1* cells respond is 3 cells (1 cell file responding). Therefore, we expect the ratio between the level of stress sensed in *atktn1* and the level in WT to be about $(3/5)^2 = 0.36$. This ratio might be slightly higher due to the variability of the response, but it is consistent with our other observations.

Model

The experimental analysis displays large variations in individual cell growth rates. In order to investigate the effect of stochasticity in cell growth rate, we sought to implement individual target growth rates in the model directly. Existing formulations are not adapted to our quest: turgor-driven models prescribe growth only indirectly as the result of the plastic deformation of cell walls under turgor pressure (Corson et al., 2009; Hamant et al., 2008), whereas the continuum approach by Coen et al. (2004) does not allow for cellular resolution. Vertex models devised for animal epithelial tissue growth offer a cell-based description (Farhadifar et al., 2007); however, the definition of a target area results in locally isotropic growth. Therefore, we generalize the vertex model approach by replacing the isotropic target area of an individual cell (numbered i) with an anisotropic target ellipse represented by a matrix $M_i^{(0)}$. We consider a single layer of cells, forming a flat polygonal tilling, where edges represent cell walls and vertices three cell contact points. The shape of a given cell yields a form matrix M_i defined as the second moment of area. Positions and shapes of cells are determined from the condition of mechanical equilibrium balancing the quest of individual cells to attain their target ellipses. This is achieved by minimizing the total energy of a tissue encompassing $i \in [1, N]$ cells.

$$E = \sum_{i=1}^{N} \left\{ \alpha P_i + \beta \left(Tr \left[M_i - M_i^{(0)} \right] \right)^2 + \chi \left(Det \left[M_i - M_i^{(0)} \right] \right)^2 \right\}.$$

By minimizing the difference in trace and determinant of actual cell form and target ellipse $M_i^{(0)}$ we ensure that the eigenvalues of the cells' form measured by M_i are the closest possible to those of the target ellipse. The additional cell perimeter P_i represents the tension in cell walls resisting turgor pressure. The minimization of the total energy with respect to cell vertex positions not only determines cell position and shape but also stresses S_i exerted by surrounding cells on individual cells. As suggested by Shraiman (Shraiman, 2005) and supported by experimental data, mechanical stresses may regulate growth. Based on the hypothesis that CMTs orient according to the highest stress, reducing growth in that direction, we investigate the effect of such a feedback on tissue growth. We explore this idea by coupling a cell's deviatoric stress D_i (defined by $D_i = S_i - 1/2 \; Tr(S_i) I$, I being the identity matrix) to its growth rate in addition to a basal growth rate $\gamma(1 \pm \sigma)$ that exhibits stochastic fluctuations of amplitude σ,

$$\frac{d}{dt} M_i^{(0)} = \gamma(1 \pm \sigma) M_i^{(0)} - \frac{\eta}{2} \left[M_i^{(0)} D_i + D_i M_i^{(0)} \right].$$

η stands for the strength of the stress feedback and quantifies the capacity of CMTs to reorient according to stress, and the speed at which this re-orientation occurs. The simulation is implemented in a custom written C++ program. Simulation parameters are chosen as $\alpha = 0.02$, $\beta = 7.0$, $\chi = 1.0$, $\gamma = 0.01$, $\eta \in [0, 15]$, $\sigma \in [0, 1]$, specifically values of $\sigma = 0.5$ and $\sigma = 0.85$ have been used in the simulations presented in Figure 5. The measure of stress anisotropy in cell i is defined by

$$SA_i = \frac{\sqrt{\left(Tr \left[S_i S_i^T \right] \right)^2 - 4 Det \left[S_i S_i^T \right]}}{Tr \left[S_i S_i^T \right]},$$

whereas stress variability is given by

$$SV_i = \sqrt{\frac{Tr \left[\left(S_i - \langle S \rangle_{nn,i} \right) \left(S_i - \langle S \rangle_{nn,i} \right)^T \right]}{Tr \left[\langle S \rangle_{nn,i} \langle S \rangle_{nn,i}^T \right]}},$$

where the average is over neighboring cells. Growth variability is defined according to the same formula. The presented statistical data is obtained with 160 independent runs of the ten iteration long growth of a tissue encompassing 126 cells.

For the implementation of cell divisions, cell division planes are chosen to go through a cell's center of mass. For the orientation of the cleavage plane, we choose either parallel orientation along the principal direction of stress or perpendicular to the principal direction of the second moment of area. Upon cell division along axis $\vec{e}$ the target matrix $M_m^{(0)}$ of the mother cell is inherited by the daughter cells $M_{di}^{(0)}$, $i = 1, 2$, according to the following rules, which ensure that in the coordinate system spanned by the division axis $\vec{e}$ and its

orthonormal partner $\vec{n}$ the parallel component of the target matrix equals the mother cell's and the perpendicular component of the mother cell is split according to the ratio of the area of the daughter A_{di} and the mother cell A_m, $e^T M_m^{(0)} e = e^T M_{di}^{(0)} e$, $n^T M_m^{(0)} n = \frac{A_{di}}{A_m} n^T M_{di}^{(0)} n$.

SUPPLEMENTAL REFERENCES

Berens, P. (2009). CircStat: A MATLAB toolbox for circular statistics. J. Stat. Softw. *31*, 1–21.

Bichet, A., Desnos, T., Turner, S., Grandjean, O., and Höfte, H. (2001). BOTERO1 is required for normal orientation of cortical microtubules and anisotropic cell expansion in *Arabidopsis.* Plant J. *25*, 137–148.

Coen, E., Rolland-Lagan, A.G., Matthews, M., Bangham, J.A., and Prusinkiewicz, P. (2004). The genetics of geometry. Proc. Natl. Acad. Sci. USA *101*, 4728–4735.

Corson, F., Hamant, O., Bohn, S., Traas, J., Boudaoud, A., and Couder, Y. (2009). Turning a plant tissue into a living cell froth through isotropic growth. Proc. Natl. Acad. Sci. USA *106*, 8453–8458.

de Reuille, P.B., Bohn-Courseau, I., Godin, C., and Traas, J. (2005). A protocol to analyse cellular dynamics during plant development. Plant J. *44*, 1045–1053.

Deveaux, Y., Peaucelle, A., Roberts, G.R., Coen, E., Simon, R., Mizukami, Y., Traas, J., Murray, J.A., Doonan, J.H., and Laufs, P. (2003). The ethanol switch: a tool for tissue-specific gene induction during plant development. Plant J. *36*, 918–930.

Dumais, J., and Kwiatkowska, D. (2002). Analysis of surface growth in shoot apices. Plant J. *31*, 229–241.

Farhadifar, R., Röper, J.C., Aigouy, B., Eaton, S., and Jülicher, F. (2007). The influence of cell mechanics, cell-cell interactions, and proliferation on epithelial packing. Curr. Biol. *17*, 2095–2104.

Fernandez, R., Das, P., Mirabet, V., Moscardi, E., Traas, J., Verdeil, J.L., Malandain, G., and Godin, C. (2010). Imaging plant growth in 4D: robust tissue reconstruction and lineaging at cell resolution. Nat. Methods *7*, 547–553.

Gennes, P.G.d., and Prost, J. (1993). The Physics of Liquid Crystals, 2nd edn (Oxford, UK: Oxford University Press).

Hamant, O., Heisler, M.G., Jönsson, H., Krupinski, P., Uyttewaal, M., Bokov, P., Corson, F., Sahlin, P., Boudaoud, A., Meyerowitz, E.M., et al. (2008). Developmental patterning by mechanical signals in *Arabidopsis.* Science *322*, 1650–1655.

Heisler, M.G., Hamant, O., Krupinski, P., Uyttewaal, M., Ohno, C., Jönsson, H., Traas, J., and Meyerowitz, E.M. (2010). Alignment between PIN1 polarity and microtubule orientation in the shoot apical meristem reveals a tight coupling between morphogenesis and auxin transport. PLoS Biol. *8*, e1000516.

Johnson, K.L. (1985). Contact Mechanics (Cambridge, UK: Cambridge University Press).

Kwiatkowska, D. (2004). Surface growth at the reproductive shoot apex of *Arabidopsis thaliana* pin-formed 1 and wild type. J. Exp. Bot. *55*, 1021–1032.

Kwiatkowska, D., and Dumais, J. (2003). Growth and morphogenesis at the vegetative shoot apex of Anagallis arvensis L. J. Exp. Bot. *54*, 1585–1595.

Landau, L.D., and Lifshits, E.M. (1970). Theory of Elasticity, 2d English edn (Oxford: Pergamon Press).

Mora, T., and Boudaoud, A. (2006). Buckling of swelling gels. Eur Phys J E Soft Matter *20*, 119–124.

Peaucelle, A., Braybrook, S.A., Le Guillou, L., Bron, E., Kuhlemeier, C., and Höfte, H. (2011). Pectin-induced changes in cell wall mechanics underlie organ initiation in *Arabidopsis.* Curr. Biol. *21*, 1720–1726.

Routier-Kierzkowska, A.-L., and Kwiatkowska, D. (2008). New stereoscopic reconstruction protocol for scanning electron microscope images and its application to in vivo replicas of the shoot apical meristem. Funct. Plant Biol. *35*, 1034–1046.

Shraiman, B.I. (2005). Mechanical feedback as a possible regulator of tissue growth. Proc. Natl. Acad. Sci. USA *102*, 3318–3323.

Smyth, D.R., Bowman, J.L., and Meyerowitz, E.M. (1990). Early flower development in *Arabidopsis.* Plant Cell *2*, 755–767.

Williams, M.H., and Green, P.B. (1988). Sequential scanning electron mi- croscopy of a growing plant meristem. Protoplasma *147*, 77–79.

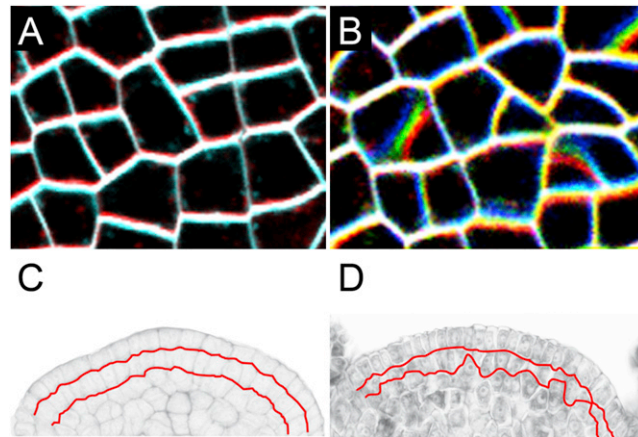Zar, J.H. (1999). Biostatistical Analysis (New Jersey: Prentice-Hall, Inc.).

Figure S1. Cell Division Plane Defects in *atktn1*, Related to Figure 1

(A and B) FM4-64-stained cell membranes at the surface of the WT (A) and *atktn1* (B) meristem taken at three Z positions (at 1 μm intervals) within the SAM epidermis and overlaid as red/green/blue image. In the WT (A), cell divisions are rather symmetric and the walls are anticlinal as demonstrated by the absence of red, green, or blue color. In the *atktn1* mutant (B), asymmetric cell divisions can be observed and oblique walls are present, as shown by the overlay.

(C and D) Median longitudinal section of WT (C) and *atktn1* (D) SAMs. The boundaries between cells from the L1, L2, and L3 have been drawn. The boundary between the L2 and L3 is ill-defined in *atktn1*, consistent with defects in cell division plane orientations in the mutant.
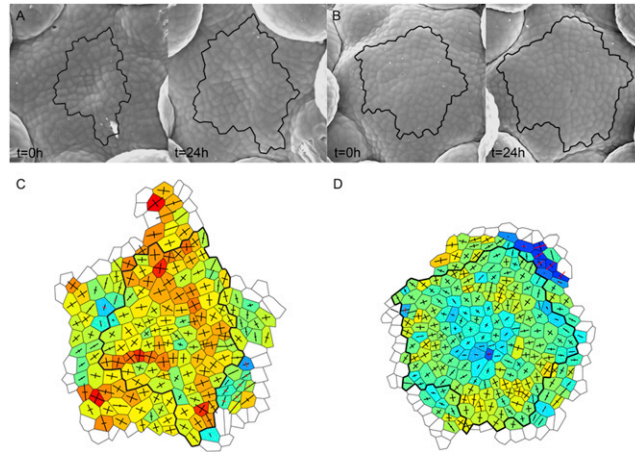
Figure S2. Differences in Growth between Two *atktn1* Meristems, Related to Figure 2

Scanning electron micrographs (A and B) and growth rate maps (C and D) of two *atktn1* meristems. The observed variability is independent of growth conditions and seems to be an intrinsic property of individual meristems.
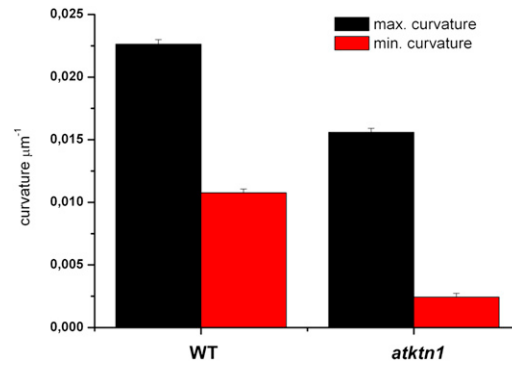
Figure S3. Mean Values of Maximal and Minimal Curvatures Computed for WT and *atktn1* SAM Cells, Related to Figure 3

Plants were grown in the Katowice laboratory conditions. Note that the mean minimal curvature is positive in *atktn1* meristems but lower than in WT. Error bars are SEM. The means computed for n = 505 cells (three meristems) of WT and n = 776 cells (three meristems) of *atktn1* are significantly different (t test, p < 0.001).
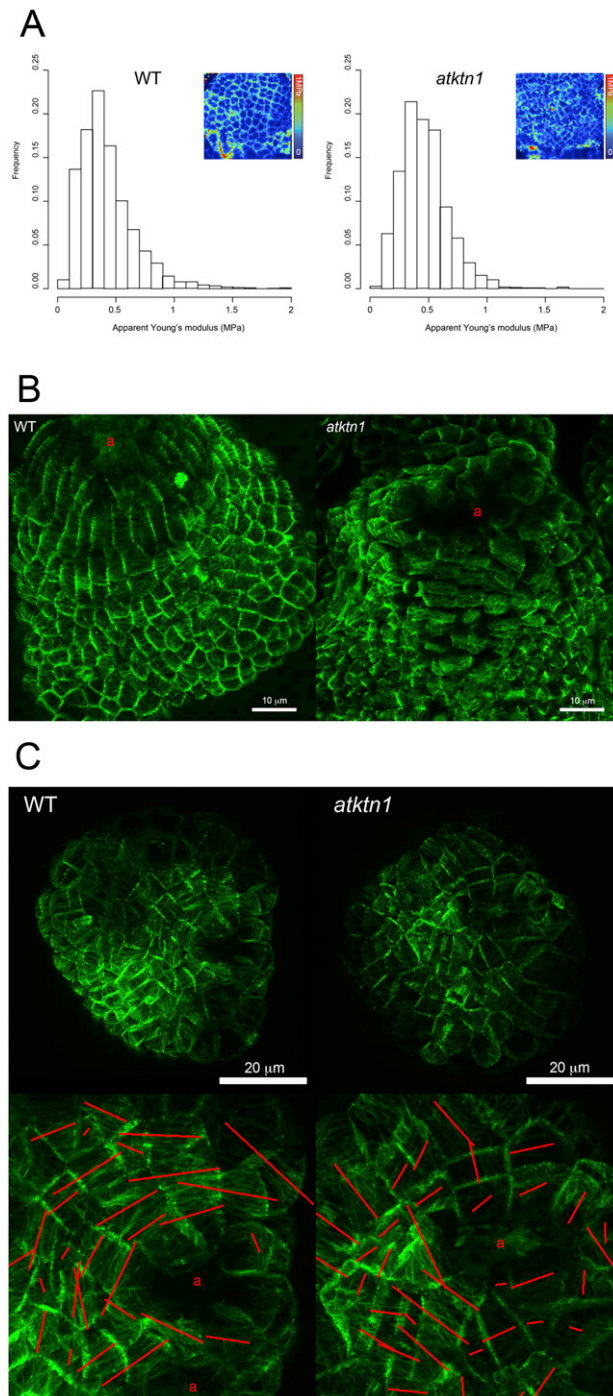
Figure S4. Mechanics in WT and *atktn1* Meristems, Related to Figure 4

(A) AFM measurement in WT and *atktn1* meristems. Distribution of the apparent Young's modulus (E_A) in the WT (n = 7 meristems, mean = 0.42 Mpa, SD = 0.24) and in *atktn1* (n = 8 meristems, mean = 0.46 Mpa; SD = 0.20; Kolmogotov-Smirnov test: p value = 0.818). A representative E_A map is shown for both genotypes. Data were collected for anticlinal walls only.

(B) WT and *atktn1* meristems 48 hr after ablation. *p35S::GFP-MBD* expression at the surface of a representative WT and *atktn1* meristems 48 hr after ablation (indicated by a). The shape of the WT SAM area surrounding the ablation site most likely results from increased growth anisotropy. These features are largely absent in the mutant.

(C) CMT response after ablation in isoxaben-treated WT and *atktn1* meristems. *p35S::GFP-MBD* expression at the surface of a representative WT (left) and *atktn1* (right) meristems 44 hr after isoxaben treatment. One or two cells (indicated by a) were wounded as their walls became more and more brittle (i.e., at least 30 hr after isoxaben treatment). The CMT response was quantified for cells surrounding the wound and visualized by red lines using the MT macro.
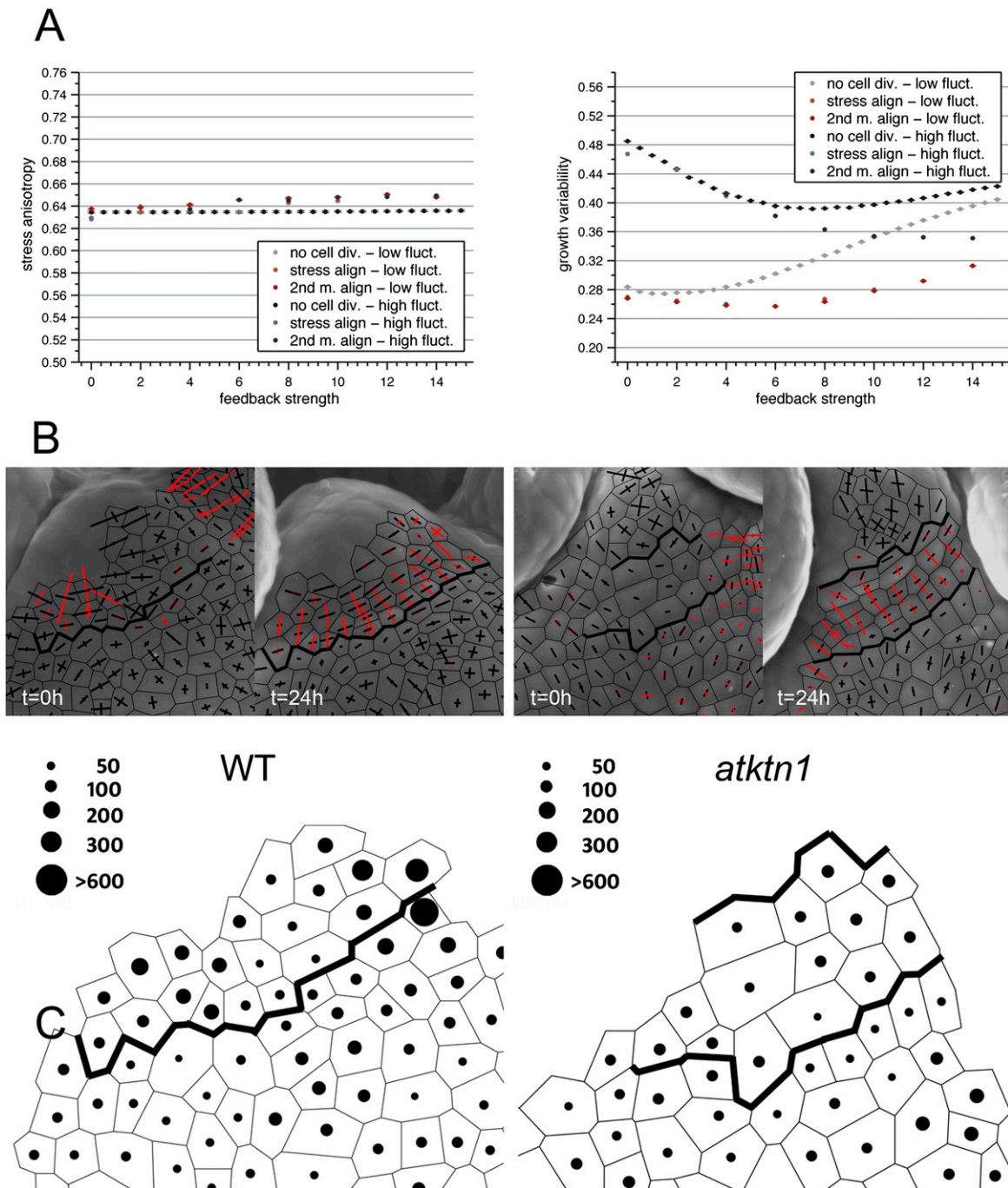
Figure S5. Impact of Mechanical Feedback on Growth, Related to Figure 5

(A) Impact of cell division on the model. See Figure 5. Including new walls in the simulation basically reinforced the stress feedback, and the growth variability curves exhibited the same shape as the ones without cell divisions, in a larger stress feedback window. New cell walls were inserted either according to the smallest cell moment (2nd m. align), corresponding roughly to the shortest wall, or according to the direction of the highest stress (stress align), consistently with the orientation of microtubules. Left panel: Stress anisotropy when stress feedback strength changes. Stress anisotropy varies between 0 (isotropic stress) and 1 (highly anisotropic stress). Including cell divisions had little influence on anisotropy. Right panel: Growth variability when stress feedback strength changes. Growth variability measures the difference in growth rate between a cell and its neighbors and takes the value 0 when all cells grow at the same rate. Including cell divisions did not affect the general trends. Error bars are SEM.

(B) Local growth variability map in WT and *atktn1*. Spatial distribution of coefficient of variability (in percents) of growth rates in the WT (left panel) and *atktn1* (right panel) meristems. The size of the disc increases with the coefficient value. Scanning electron micrographs with overlaid principal curvature directions for both genotypes are included. Regions that will give rise to boundaries (creases with a negative curvature in meridional direction) during the next 24 hr are delineated with thick lines.